THESIS FOR THE DEGREE OF DOCTOR OF PHILOSOPHY

Characterization methods and modelling for Li-ion batteries

entropy, impedance, pressure, diffusivity & temperature swings induced aging

Zeyang Geng

Department of Electrical Engineering
Chalmers University of Technology
Gothenburg, Sweden, 2022

Characterization methods and modelling for Li-ion batteries
entropy, impedance, pressure, diffusivity & temperature swings induced aging

Zeyang Geng
ISBN 978-91-7905-655-1

Doktorsavhandlingar vid Chalmers tekniska högskola
Ny serie nr. 5121
ISSN 0346-718X

Department of Electrical Engineering
Chalmers University of Technology
SE-412 96 Gothenburg, Sweden
Phone: +46 (0)31 772 1000
www.chalmers.se

This thesis has been prepared using LaTeX.
Printed by Chalmers Reproservice
Gothenburg, Sweden, May 2022

Abstract

Lithium-ion batteries are commonly used for energy storage systems, and temperature is one key impact factor on the cell performance and lifetime. In literature, the focus has been on the ambient temperature of the test condition, and there is little discussion about how the temperature swing during cycling affects the battery lifetime. In this study, lithium-ion cells are cycled with the same current but different temperature swings for more than two years. The results show that the cells cycled with a high temperature swing aged faster. Moreover, pure thermal cycling does not introduce significant aging to the cell.

During the study, a series of characterization methods were also developed, including a physics-based circuit model, a convenient method to measure the entropic coefficient, an on-line impedance measurement technique, an effective reference performance test procedure, and methods to measure the cell pressure and thickness change during cycling. A selection of results are that the physics-based circuit model could predict key quantities, such as overpotential, concentrations etc., with less than 0.05% deviation compared with a state-of-art model. Furthermore, the on-line impedance measurement technique managed to extract the battery pack impedance between 0.01 Hz and 5 Hz based on CAN signals. In addition, the cell pressure and thickness change during cycling of a commercial cell were found to be up to 60 kPa and 150 μm.

Keywords: Li-ion batteries, temperature swing, aging, lifetime, characterization methods, model, impedance, entropy, thermal, pressure, swelling.

Acknowledgments

First of all, I would like to thank Torjörn Thiringer, my supervisor, examiner, mentor, and friend, who never let me down. Thank you for your continues support and wise guidance. I would also like to thank my co-supervisor, Daniel Brandell at Uppsala University, who opened the door for me to the world of electrochemistry and material science. Thank you for hosting me at Ångströmlaboratoriet and for your feedback along the way, which is always fast and detailed.

I am also grateful to the people in the reference group of this project: Jens Groot, Polestar, who is the first person that taught me how to test batteries during my master study, and I can always learn something new every time when we work together; Matthew J. Lacey, Scania, from whom I got most of the inspirations to bridge the gap between electrical engineering and electrochemistry; Kristian Frenander, Volvo Cars, and Tomas Tengner, ABB, for fruitful discussions during the meetings. A special thank to Siyang Wang, who has never worked with batteries before, but devoted his mathematical skills in solving the electrochemical equations accurately and elegantly.

Thanks to Felix Mannerhagen and Douglas Jutsell Nilsson for helping and teaching me about the mechanical manufacturing needed for building the experiment setups. Thanks also go to my colleagues at Elkraftteknik. It has been a great pleasure to have your company along this journey.

Finally, I would like to express my appreciation to Sweden Energimyndigheten and Hans-Olof Dahlberg for the financial support to the thesis work, especially for the opportunity of building our in-house test facility. Moreover, I would like to thank Chalmers Areas of Advance for financing a series of small projects to develop our ideas.

Acronyms

AI:	Analog Input
AIOS:	Auxiliary Input & Output System
CAN:	Controller Area Network
CCCV:	Constant Current Constant Voltage
DO:	Digital Output
DVA:	Differential Voltage Analysis
ECM:	Equivalent Circuit Model
EIS:	Electrochemical Impedance Spectroscopy
FCE:	Full Cycle Equivalent
FFT:	Fast Fourier Transform
FSD:	Full Scale Deviation
GITT:	Galvanostatic Intermittent Titration Technique
GPIB:	General Purpose Interface Bus
ICA:	Incremental Capacity Analysis
ICI:	Intermittent Current Interruption
LPN:	Lumped Parameter Network
OBD:	On-board Diagnostic
OCV:	Open Circuit Voltage
PRBS:	Pseudo-Random Binary Sequences
RTD:	Resistance Temperature Detector
RPT:	Reference Performance Test

SEI:	Solid Electrolyte Interphase
SOC:	State of Charge
SOH:	State of Health
TS:	Temperature Swing

Nomenclature

Symbols

α	Transfer coefficient
ϵ	Volume fraction
η	Overpotential caused by the redox reaction, V
κ	Electrolyte conductivity, S/m
λ	Positive roots of $\lambda = \tan(\lambda)$
Φ	Electrical potential, V
ρ	Density, kg/m^3
σ	Electrode conductivity, S/m
A	Area, m^2
C	Heat capacity, J/K
c	Lithium ion concentration, mol/m^3
c_0	Initial concentration in the intercalation material, mol/m^3
C_s	Specific heat capacity, J/kg·K
$c_{s,max}$	Maximum concentration in the intercalation material, mol/m^3
$c_{s,surf}$	Lithium ion concentration on the particle surface, mol/m^3
D	Diffusion coefficient, m^2/s
d	Thickness, m
dU/dT	Entropic coefficient, V/K
E	Voltage, V
F	Faraday constant, 96485 s·A/mol
f_A	Activity coefficient of the salt

G	Gibbs free energy, J
H	Enthalpy, J
h	Heat transfer coefficient, W/m^2·K
I	Given current density, A/m^2
i	Current density per electrode area, A/m^2
I_{batt}	Current in the outer circuit, A
j	Charge transfer current density per surface area, A/m^2
j_0	Exchange current density, A/m^2
k	Thermal conductivity, W/m·K
k_a	Anodic reaction rate constant
k_c	Cathodic reaction rate constant
L	Electrode thickness, m
n	Number of electrons involved in the redox reaction
P	Pressure, Pa
Q_{irr}	Irreversible heat, W
Q_{rev}	Reversible heat, W
R	Gas constant, 8.314 J/mol·K
r	Radial distance in the particle, m
R_l	Electrolyte resistance, Ω·m^2
R_s	Electronic resistance in the solid, Ω·m^2
r_s	Radius of solid particles, m
R_{ct}	Charge transfer resistance, Ω·m^2
R_{th}	Thermal resistance, K/W

S	Entropy, J/K
S_a	Specific surface area, m^2/m^3
T	Temperature, K
t	Time, s
t_+^0	Transference number of lithium ion
T_{amb}	Ambient temperature, K
U	Electrode potential, V
V	Voltage, V
Vol	Volume, m^3
x	Stoichiometry, $x = c_s/c_{s,max}$
Z	Impedance Ω
Z_w	Warburg impedance, $\Omega \cdot m^2$

Subscripts

0	Initial condition
a	Anodic
c	Cathodic
$imag$	Imaginary part of a complex number
l	Liquid phase
neg	Negative electrode
pos	Positive electrode
$real$	Real part of a complex number
s	Solid phase
sep	Separator

Superscripts

eff	Effective

List of Publications

This thesis is based on the following publications:

[I] **Z. Geng**, J. Groot, T. Thiringer, "A time- and cost-effective method for entropic coefficient determination of a large commercial battery cell". *IEEE Transactions on Transportation Electrification*, March 2020, doi: 10.1109/TTE.2020.2971454.

[II] **Z. Geng**, S. Wang, M. J Lacey, D. Brandell, T. Thiringer, "Bridging physics-based and equivalent circuit models for lithium-ion batteries". *Electrochimica Acta*, March 2021, doi: 10.1016/j.electacta.2021.137829.

[III] **Z. Geng**, T. Thiringer, M. J Lacey, "Intermittent current interruption method for commercial lithium ion batteries aging characterization". *IEEE Transactions on Transportation Electrification (Early Access)*, doi: 10.1109/TTE.2021.3125418.

[IV] **Z. Geng**, Y.C. Chien, M. J Lacey, T. Thiringer, D. Brandell, "Validity of solid-state Li^+ diffusion coefficient estimation by electrochemical approaches for lithium-ion batteries". *Electrochimica Acta*, December 2021, doi: 10.1016/j.electacta.2021.139727.

[V] **Z. Geng**, T. Thiringer, "In situ key aging parameter determination of a vehicle battery using only CAN signals in commercial vehicles". *Applied Energy*, May 2022, doi: 10.1016/j.apenergy.2022.118932.

Other publications by the author, not included in this thesis, are:

[VI] **Z. Geng**, T. Thiringer, Y. Olofsson, J. Groot, M. West, "On-board impedance diagnostics method of Li-ion traction batteries using pseudo-random binary sequences". *20th European Conference on Power Electronics and Applications (EPE'18 ECCE Europe)*, Riga, Latvia, Sept. 2018.

[VII] A. Kersten, M. Kuder, E. Grunditz, **Z. Geng**, E. Wikner, T. Thiringer, T. Weyh, R. Eckerle, "Inverter and battery drive cycle efficiency comparisons of chb and mmsp traction inverters for electric vehicles". *21st European*

Conference on Power Electronics and Applications (EPE '19 ECCE Europe), Genova, Italy, Sept. 2019. doi: 10.23919/EPE.2019.8915147.

[VIII] **Z. Geng**, F. Mannerhagen and T. Thiringer, "Characterization of lithium ion supercapacitors". *22nd European Conference on Power Electronics and Applications (EPE'20 ECCE Europe)*, Lyon, France, Sept. 2020. doi: 10.23919/EPE20ECCEEurope43536.2020.9215710.

[IX] J. Xu, **Z. Geng**, M. Johansen, D. Carlstedt, S. Duan, T. Thiringer, F. Liu, L. Asp, "A multicell structural battery composite laminate". EcoMat. 2022, doi: 10.1002/eom2.12180.

[X] L. Yin, **Z. Geng**, A. Björneklett, E. Söderlund, T. Thiringer, D. Brandell, "An integrated flow-electric-thermal model for a cylindrical Li-ion battery module with a direct liquid cooling strategy". *Under review.*

[XI] L. Yin, **Z. Geng**, Y.C. Chien, T. Thiringer, M.J. Lace, A.M. Andersson, D. Brandell, "Implementing intermittent current interruption into Li-ion cell modelling for improved battery diagnostics". *Under review.*

Contents

CHAPTER 1

Introduction

1.1 Background

Lithium (Li) ion batteries are commonly used in energy storage systems with the advantage of having both high energy density and high power density. However, the lifetime of Li-ion batteries is often the limiting factor of the systems' lifespan, depending on the usage conditions. A better understanding of how the usage condition affects the battery lifetime can provide a guidance when designing a battery system to operate the battery in its favoured condition, and thus prolong the battery lifetime.

There are multiple factors during a battery usage that can affect its lifetime, including voltage window, current magnitude, cell temperature and external pressure. When it comes to the cell temperature, previous studies have shown that Li-ion cells favour room temperature, while both a very high or low temperature will accelerate the cell aging [1], [2]. During charging or discharging, the cell heat generation will lead to a temperature rise and later the temperature falls back towards the ambient temperature during idling. Most of the reported studies have been focusing on the ambient temperature [3]–[5] whereas the temperature swing (TS) during the cell usage has been less tar-

geted.The temperature swing is the main aging factor for power electronics [6], [7] and also of great importance for aging of electric machines [8], while similar studies for Li-ion batteries are lacking.

In a fast charging study prior to this work, a Li-ion cell (of the same type as what will be used in this work) was placed in a well thermal isolated setup to mimic the environment in a battery pack. Different current levels up to 5C were used to cycle the cell in room temperature. The resulting voltages and temperatures are presented in Fig. 1.1. It can be noted that the temperature development under a high current is significant, especially during discharging. The accelerated aging process due to a high C-rate is well-known [9], however it is uncertain to which extent it is related with the current itself or the temperature increase caused by the current, since the current and temperature are directly coupled. One recent study showed that an asymmetric temperature pattern with an elevated temperature during fast charging can prolong the battery lifetime significantly [10].

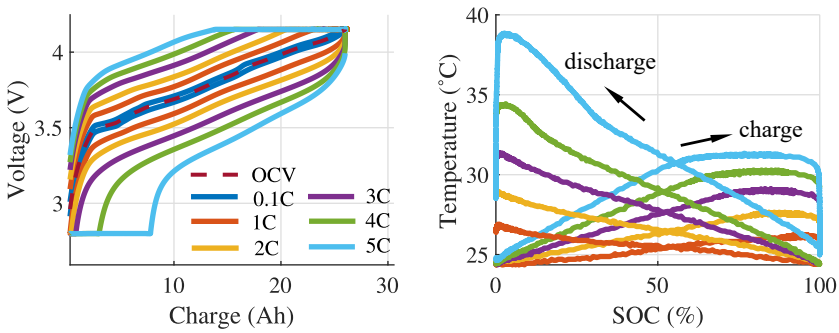

Figure 1.1: The cell temperature development during fast charging.

A better understanding about how the temperature swing affects battery aging does not only benefit the lifetime with a better system design, but also help conducting more relevant aging testing to predict the battery lifetime before production. So far, the battery lifetime prediction still relies on massive aging testing performed in the factory or laboratory, where only the ambient temperature is controlled. Without considering and controlling the resulting temperature swings, the aging results might be misleading.

In this work, a special test setup is designed, utilizing different thermal insulation and additional heating to create symmetric temperature swings with the same current magnitude. With this setup, the impact of current and temperature swing on battery aging can be decoupled and investigated. During this study, a series of Li-ion cell characterization methods were developed as a complement to the main aging study.

1.2 Aim

The aim of this work is to investigate how the temperature swings during cycling affect the lifetime of Li-ion batteries. Furthermore, an important target is to develop and validate characterization methods for commercial Li-ion cells, which for instance can be used to track cell degradation.

1.3 Contributions

The main project task contributions are

- Development of experiment setups to create different temperature swings with the same current, ambient and average temperatures. In this setup, the temperature distribution on the cell surface and the contact resistance on the cell terminals are monitored as supplementary information.
- Description of using a battery tester without an integrated function to perform in-situ electrochemical impedance spectroscopy (EIS) measurement at frequencies lower than 100 Hz.
- Demonstration of the impact of temperature swings on the battery lifetime based on experimental results.

Additional contributions in this thesis work are[1]

- Concept development, implementation, and validation of a time and cost effective methods to measure the entropic coefficient dU/dT for large format Li-ion batteries (**Paper I**).

[1] Background, scoping and niche building for the additional contributions can be found in the introductions of respective articles.

- Development of a physics-based electrochemical model with a transmission line structure to bridge the equivalent circuit model and the physical principles, as well as a validation of the model towards COMSOL Multiphysics (**Paper II**).
- Implementation and verification of an effective reference performance test (RPT) containing an intermittent current interruption (ICI) method for Li-ion battery aging test (**Paper III**).
- Theory validation of galvanostatic intermittent titration technique (GITT) and ICI for their application in Li-ion porous electrodes (**Paper IV**).
- Development and verification of a methodology to conduct electrochemical impedance spectroscopy (EIS) using only commonly CAN signals and on-board equipment on a commercial electrified vehicle (**Paper V**).
- Demonstration of two test setups to measure the pressure and volume change of Li-ion cells during cycling.

1.4 Thesis outline

This thesis is arranged as the following:

Chapter 2 introduces the theory of Li-ion batteries and the aging mechanism. A modelling work **Paper II** is presented in this chapter.

Chapter 3 is a collection of characterization methods for Li-ion batteries, as a result extension from this thesis work, based on **Paper I**, **III**, **IV**, and **V**.

Chapter 4 explains the experimental setup for the aging test to investigate how the temperature swing affects the battery lifetime, which is the main purpose of this thesis work.

Chapter 5 presents the aging results with different temperature swings. The conclusions and future work are discussed in Chapter 6.

CHAPTER 2

Li-ion batteries and modelling

2.1 Li-ion batteries

There are mainly three types of commercial Li-ion cells packing: pouch cells, prismatic cells, and cylindrical cells. All three types can be found in various types of electric vehicles. Pouch cells are more compact compared to the other two types as there is no hard casing in the cell packaging. The pouch cell used in this work is assembled with Z-stacking, where the separator is Z-folded and the electrodes are stacked [4]. For simplification, one example of single sheet stacking is shown here in Fig. 2.1. With the stacking configuration, a commercial pouch cell is formed with multiple electrochemical cells connected in parallel. One electrochemical cell consists of 5 parts, as shown in Fig. 2.2:

1. The current collector on the negative side is often made of copper. Although aluminium is lighter and cheaper than copper, it is unstable at a lower potential. The negative terminal tab is often coated with nickel on the surface to avoid corrosion.

2. Negative electrode. The most common negative electrode material is graphite. Besides, silicon-graphite (SiC) and lithium-titanium-oxide

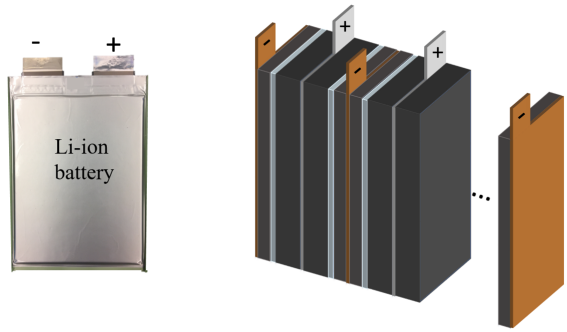

Figure 2.1: One example of the pouch cell assembly.

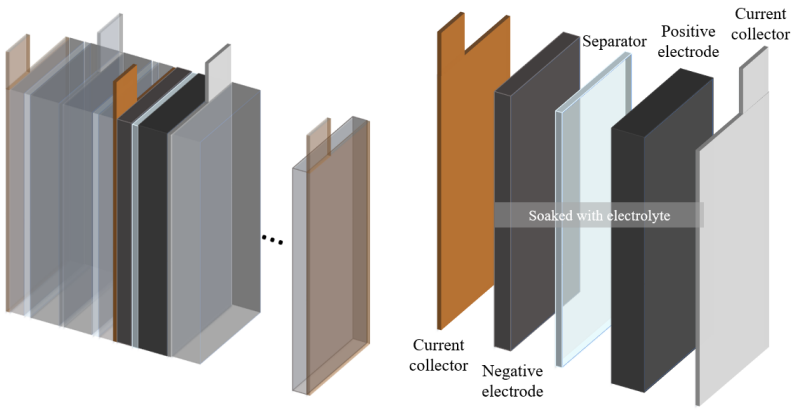

Figure 2.2: One electrochemical cell inside a pouch cell.

(LTO) can also be found in commercial cells.

3. Separator. The separator is an electric insulator while it allows ionic transport.

4. Positive electrode. In contrast to the limited choices of the negative electrode material, there are rather many options for the positive electrode materials, including $LiFePO_4$, $LiCoO_2$, $LiMn_2O_4$, $LiNi_{0.8}Co_{0.15}Al_{0.05}O_2$, $LiNi_xMn_yCo_zO_2$ (x+y+z=1, x:y:z = 1:1:1, 5:2:3, 6:2:2, 8:1:1.),...

5. Current collector on the positive side, often made of aluminium.

Both the separator and electrodes are porous materials and soaked in electrolyte. The electrolyte provides a path for the current via ionic transport inside the cell, which forms a closed circuit loop together with the electronic transport in the outer circuit.

The battery cells used in this project are Li-ion pouch cells where the positive electrode is a mixture of $LiNi_{0.33}Mn_{0.33}Co_{0.33}O_2$ (NMC111) and $LiMn_2O_4$ (LMO), and the negative electrode is graphite [4]. The capacity of the cell is 26 Ah and the size is approximately 200 mm $\times$ 150 mm $\times$ 7 mm.

2.2 Continuum modelling

The Doyle-Fuller-Newman (DFN) model was developed in early 90's as the classic continuum model for Li-ion batteries [11]. The equations used in the DFN model are summarized in Table 2.1. In this model, the mass transfer in the electrolyte is described with the concentrated electrolyte theory given in (2.7) and (2.3). The solid-state diffusion and charge transfer reactions are modeled with Fick's laws of diffusion, found in (2.8), and the Butler–Volmer equation, expressed in (2.4), respectively. The effective transport parameters in the porous materials are calculated with the porosity and an equivalent Bruggeman constant in (2.9).

This model is built upon first principles, and it is often compared with an equivalent circuit model (ECM) consisting of resistors and capacitors. Although the ECM is considered as an empirical approach, it has the advantage of being easy to interpret and implement. To bridge these two types of model, a physics-based model with a circuit structure was proposed in **Paper II**. The circuit is based on the transmission line structure shown in Fig. 2.3, which can describe the current distribution within the porous electrodes while each electrochemical processes are represented with electrical circuit elements.

This model has been validated against COMSOL Multiphysics, a commercial software based on the finite element method. The results show that the deviation between the proposed model and COMSOL is below 0.05% most of the time, and maximum 0.5% if a coarse mesh is used. The source code can be downloaded via

`https://github.com/SiyangWangSE/CircuitModelLi-ionBattery`.

Table 2.1: Equations used in the DFN model.

	Equations with boundary conditions		Implementation
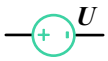	$U = U(c_{s,surf})$	(2.1)	Update the voltage source
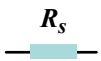	$i_s = -\sigma_s^{eff} \nabla \Phi_s$	(2.2)	Update the electrode resistance $R_s = -h\nabla\Phi_s / i_s$
	$\nabla \Phi_s = -I/\sigma_s^{eff}$ at $x = 0$ and $x = L$		
	$\vec{i}_l = -\kappa^{eff} \nabla \Phi_l + \frac{2\kappa^{eff} RT}{F}(1 + \frac{\partial ln f_A}{\partial ln c_l})(1 - t_+^0)\nabla ln c_l$	(2.3)	Update the electrolyte resistance $R_l = -h\nabla\Phi_l / i_l$
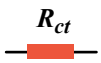	$j = j_0(exp\frac{\alpha_a F\eta}{RT} - exp\frac{-\alpha_c F\eta}{RT})$	(2.4)	Update the charge transfer resistance $R_{ct} = \eta / S_a hj$
	$j_0 = F k_c^{\alpha_a} k_a^{\alpha_c} (c_{s,max} - c_{s,surf})^{\alpha_a} c_{s,surf}^{\alpha_c} c_l^{\alpha_a}$		
Current distribution	$I = \vec{i}_s + \vec{i}_l$	(2.5)	Mesh current method
	$S_a j = \nabla \cdot \vec{i}_l$	(2.6)	Mesh current method
Concentration distribution	$\epsilon_l \frac{\partial c_l}{\partial t} = \nabla \cdot (\epsilon_l D_l^{eff} \nabla c_l) - \frac{\vec{i}_l \cdot \nabla t_+^0}{F} + \frac{S_a j(1 - t_+^0)}{F}$	(2.7)	Finite difference method
	$\nabla c_l = 0$ at $x = 0$ and $x = L$		
	$\frac{\partial c_s}{\partial t} = D_s(\frac{\partial^2 c_s}{\partial r^2} + \frac{2}{r}\frac{\partial c_s}{\partial r})$	(2.8)	Finite difference method
	$\frac{\partial c_s}{\partial r} = 0$ at $r = 0$, $\frac{\partial c_s}{\partial r} = -FD_s/j$ at $r = r_s$		
Porous electrode	$\sigma_s^{eff} = \sigma_s \epsilon_s^{1.5}$, $\kappa^{eff} = \kappa \epsilon_l^{1.5}$, $D_l^{eff} = D_l \epsilon_l^{1.5}$	(2.9)	

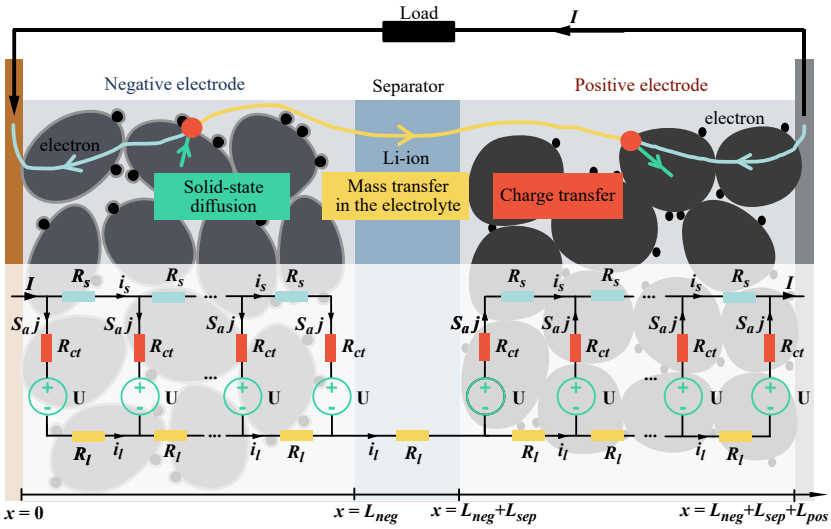

Figure 2.3: A schematic of the transmission line structure.

2.3 Aging mechanism

As described above, the battery is a complex electrochemical system and the aging mechanism is even more complicated [12]. The battery aging is reflected in terms of the fading in capacity and the increase in resistance [13]. When the capacity of the battery decreases to 80% of its initial capacity, the battery is considered to reach its end of life for automotive applications. The capacity is often defined as the discharge capacity under a certain C-rate, therefore both a loss of lithium inventory and an increased resistance can result in capacity fading.

One of the main aging mechanism in Li-ion batteries is the formation of the solid electrolyte interphase (SEI), which is both a protection layer and a degradation factor [14]. The SEI forms when the negative electrode is outside of the electrolyte stability window, starting the first time when the cell is being charged. This process will continue in each cycle to form a thicker and thicker SEI layer. A similar reaction occurs on the positive electrode as well [15]. The formation of the SEI layer will cause both a loss of lithium inventory and a resistance increase. This side reaction of SEI formation is faster at a higher

temperature and higher potential, which explains why a severe calendar aging is often observed when the cells are stored at high temperature and high state of charge [16].

Another aging mechanism is the lithium plating, which is a safety concern as well, especially during fast charging at a low temperature. Therefore, during fast charging, an elevated temperature is sometimes preferred. With an elevated temperature, the overpotential is reduced, which can avoid unwanted side reactions [10].

Moreover, the mechanical force introduced by the material can cause particle cracking [17]. This will expose new electrode surfaces to form new SEI layers and thus consume cyclable lithium ions. Moreover, it can cause loss of active materials due to the loss of electrical contact. One question to be answered in this work is whether a temperature swing, i.e. a thermal stress can cause a notable mechanical stress and then result in a notable degradation.

CHAPTER 3

Characterization methods

3.1 Equipment overview

- *Cell tester PEC ACT0550*

  This is the main tester used in this thesis work. The power range of a single channel is up to 5 V, 50 A. The channels can be paralleled to achieve a higher current range. The maximum sampling frequency is 1 kHz but it can only operate for a short time with such a high sampling rate, limited by the transmission buffer. Each channel includes a temperature input for one RTD (Resistance Temperature Detector) sensor, for example a PT100 sensor.

  The main tester can interact with its AIOS (Auxiliary Input Output System) via CAN (Controller Area Network) so that extra input/output and temperature signals can be added in the main channel. In this thesis work, analog inputs, digital outputs, and type K thermocouples are used in the system. The tester can also control temperature chambers, for example the two Espec LU124 used in this work, via Ethernet.

- *Potentiostat GAMRY Reference 3000AE*

The GAMRY Reference 3000 is a high accuracy potentiostat. The power range is 32 V/1.5 A or 15 V/3 A. The current can be boosted to maximum 30 A with an external booster. It can perform an EIS measurement up to 1 MHz. The default maximum sampling frequency is 1 kHz and with modified software it can reach 10 kHz. There are 8 auxiliary analog measurement channels and it can be used to for battery pack or module testing.

- *DAQ system (data acquisition) Ipetronik and its software IPEmotion*

  the Ipetronik M-thermo 16 and M-thermo 8 have been used in this thesis work to acquire temperature signals with type K thermocouples. Besides, M-sens 8 and M-sens 4 are used to acquire analog signals. The M-sens series can also provide a voltage supply for the sensors but with a limited current supply. All the Ipetronik devices can be interconnected via CAN and then connected to the computer with a CAN interface. The maximum logging frequency is 2 kHz.

- *Bench multimeter HP/Agilent 34401A*

  It is a high resolution analog measurement device, and it has been used in the project to measure the entropic coefficient of Li-ion batteries. It can interact with MATLAB software via either RS232 or GPIB.

The input impedance of the equipment mentioned above is between 1 MΩ and 10 MΩ, meaning that there will be a leakage current around a few μA in the system when a cell is connected. Since the experiments presented in this thesis were performed on large format commercial cells (26 Ah), this leakage current will not introduce significant errors in the measurement. However, if these equipment are to be used with three-electrode setups, a leakage current through the reference electrode could be a problem. More detailed technique specifications about the equipment can be found in Appendix A.

3.2 Electrical characterization

Electrochemical impedance spectroscopy (EIS)

A Li-ion cell is a non-linear component and its impedance varies at different frequencies. Often the technique electrochemical impedance spectroscopy

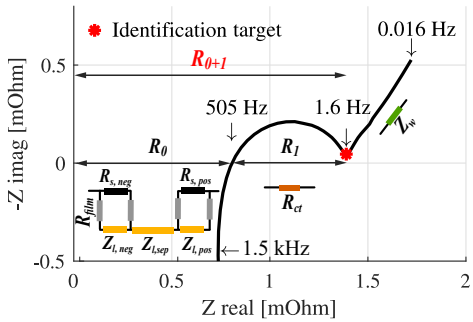

Figure 3.1: One example of the impedance of a Li-ion battery measured with a GAMRY reference 3000 and how it can be interpreted with electrochemical processes.

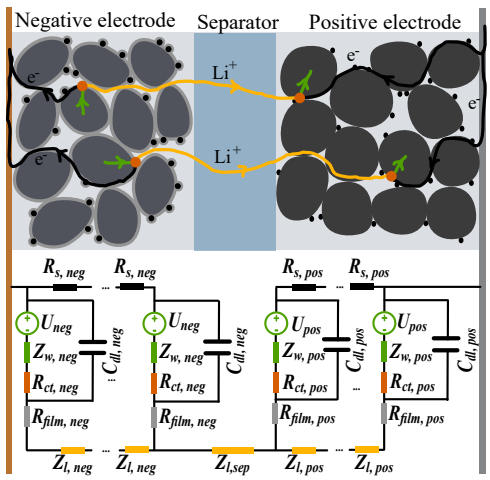

Figure 3.2: Electrochemical processes inside the battery to related with the EIS measurement.

(EIS) is used to measure the frequency dependent impedance. One example of the battery impedance is shown in Fig. 3.1. The interpretation of the EIS plot is ambiguous when it comes to porous Li-ion cells since the system is coupled

with multiple electrochemical processes. One attempt to interpret the EIS results can be found in Fig. 3.1 and Fig. 3.2, based on the transmission line model.

The impedance of the battery is affected by the cell temperature, current magnitude, current direction, its state of charge, as well as its state of health. Therefore it is a powerful diagnostic tool for Li-ion batteries aging. The identification target, R_{0+1}, is a signature value in the EIS results, which can be used as a state of health indicator. To perform an in-situ EIS measurement on a battery pack, with typically 400 V in an electric vehicle, is very challenging, as the potentiostat used in laboratory for EIS measurement has a very limited voltage range.

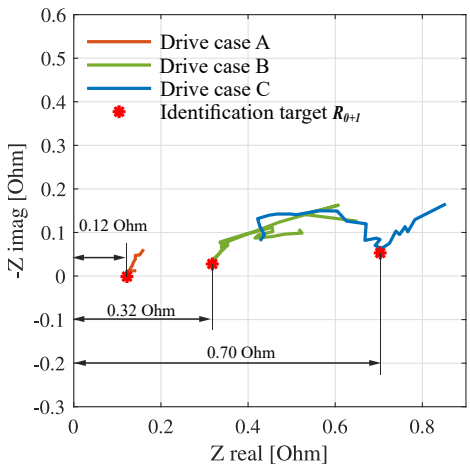

Figure 3.3: EIS plot of the battery pack computed directly using the on-board data in three drive cases.

Table 3.1: Identified R_{0+1} with driving cycles in different conditions.

Drive case	R_{0+1}
Drive case A: 22 % SOC, 23 ^{o}C	0.12 Ohm
Drive case B: 78 % SOC, 2.5 ^{o}C	0.32 Ohm
Drive case C: 21 % SOC, -10 ^{o}C	0.70 Ohm

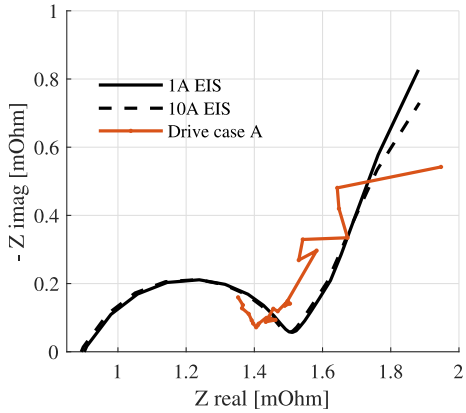

Figure 3.4: A verification of the measured EIS with on road driving data in a laboratory environment.

Besides the classic approach for the EIS measurement, which is to apply a series of sinusoidal waves with a frequency sweep, there exist other diagnostic methods, for example to apply a current signal that contains sufficient harmonics. The information in the frequency domain of a time-series measurement can be extracted with Fourier analysis and be used to identify the cell impedance. The input signal in the time domain can either be a designed time-series signal sequence, for example a PRBS (pseudo-random binary sequences) signal [18], or it can be a signal acquired from a random driving pattern. The time-series measurement has a relatively lower requirement on the hardware and it can be performed with on-board equipment.

In **Paper V**, an electrified test vehicle was driven on the road, and the CAN bus data was obtained via the OBD (on-board diagnostic) connector and then analysed with FFT (fast Fourier transform). The results show that the current signal on the battery during a normal driving contains sufficient harmonics, which can be utilized to extract the battery impedance during driving. The vehicle was driven at different ambient temperatures and different states of charge. The extracted impedance can clearly reflect the different test conditions (Table 3.1), shown in Fig. 3.3. The current pattern during

the on road driving was recorded and reproduced with the PEC ATC0550 and a paralleling kit in a laboratory environment, and then applied on a battery cell which is the same type of cell as what is used in the test vehicle. The verification results in Fig. 3.4 proves the validity of this approach. This work is a full validation of the test methods, from concept development to the implementation and verification in a real industrial product.

Intermittent current interruption (ICI)

Although the EIS technique is powerful, it requires advanced equipment which might not be available, or not applicable due to its limited voltage range. Moreover, the cell is preferred to be under an equilibrium state. Besides the complications in the measurement, the interpretation in Fig. 3.1 and 3.2 are intuitive and in reality it is very difficult to separate different electrochemical processes based on the EIS result. On the other hand, it is often sufficient to obtain a few key values for the electrical characters of a Li-ion cell, and this can be achieved with the ICI method.

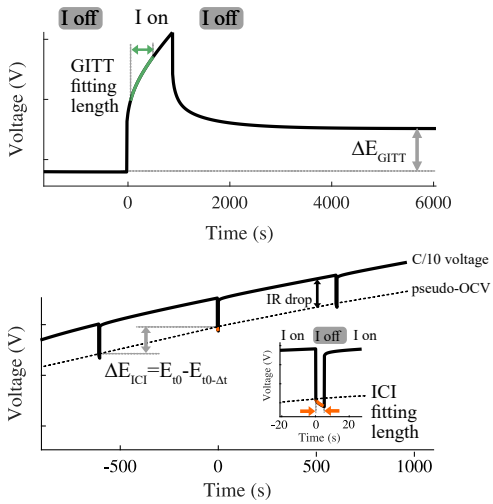

Figure 3.5: An illustration of the ICI method.

In this method, a constant current is applied on the cell and then it is interrupted for a short period, typically for a few seconds, at different states

of charge. The voltage response during the current interruption is used to calculate the resistive and diffusive properties of the cell, as shown in Fig. 3.5 and Fig. 3.6.

The voltage response during the interruption follows a linear relationship of the square root of time, similar as in the GITT method. The slope in this linear relationship $dV/d\sqrt{t}$ is related with the Li^+ solid-state diffusion coefficient D_s. This has been validated both experimentally in [19] and theoretically in **Paper IV**. The voltage drop when the current is interrupted can be used to calculate the resistive component, shown in Fig. 3.6. With a linear regression method proposed by Lacey in [20], the regression resistance is equivalent to $R_0 + R_{ct}$ in the EIS results, which is experimentally validated in [20] and **Paper III**.

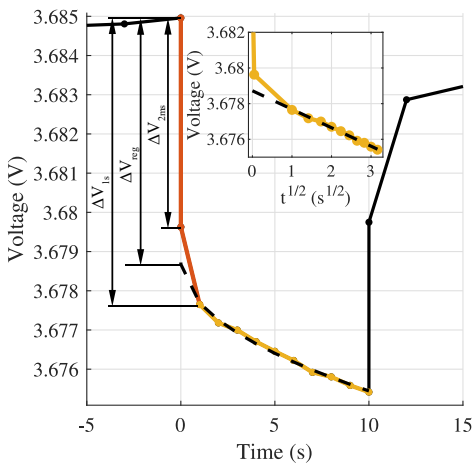

Figure 3.6: The voltage response during the current interruption in the ICI method.

Besides the resistive and diffusive properties, the voltage during the charge and discharge cycles can be used to provide data for incremental capacity analysis (ICA) and differential voltage analysis (DVA) since the short interruptions do not introduce significant distortions in the voltage profile. The ICI method is useful and practical, which has the potential to be implemented in a system, for example an electric vehicle or a stationary storage system, to track the battery aging. The discussion about the requirements on the system

level was presented in **Paper III**.

3.3 Thermal characterization

Similarly as for many other electric devices, the temperature is a key impact factor for Li-ion batteries in terms of performance and life time. What is different is that the heat source from a Li-ion cell consists of two parts, the irreversible heat loss which is mainly due to the overpotential, and the reversible heat which is related with the entropy change, illustrated in Fig. 3.7.

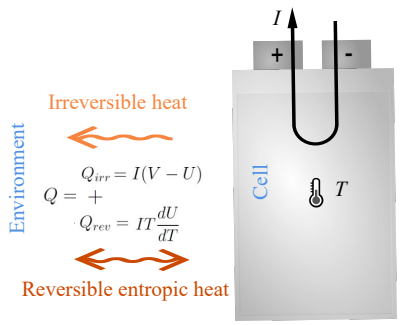

Figure 3.7: Heat generation in a lithium ion battery cell.

Irreversible ohmic heat loss

When a Li-ion battery is not at its equilibrium state, there exist overpotentials caused by electrochemical processes presented in Fig. 2.3, which will create irreversible heat losses

$$Q_{irr} = I(V - U) \tag{3.1}$$

where V is the cell terminal voltage and U is the voltage at the equilibrium state, so called open circuit voltage. The cell impedance $Z = (V - U)/I$ is normally lower at a higher current, high SOC, and higher temperature.

Reversible entropic heat

The reversible heat

$$Q_{rev} = IT\frac{dU}{dT} \tag{3.2}$$

is related with the temperature coefficient dU/dT. The coefficient itself is a material property, reflecting the vibration entropy and configuration entropy [21] where the configuration entropy is dependent on the stoichiometry x in the electrode material.

The reversible heat is dominating the total heat generation when the current is low and therefore must be included in the thermal modelling to achieve an accurate estimation of the cell temperature. Moreover, it has been suggested that the temperature coefficient profile can be a useful indicator for the SOH diagnostic [22].

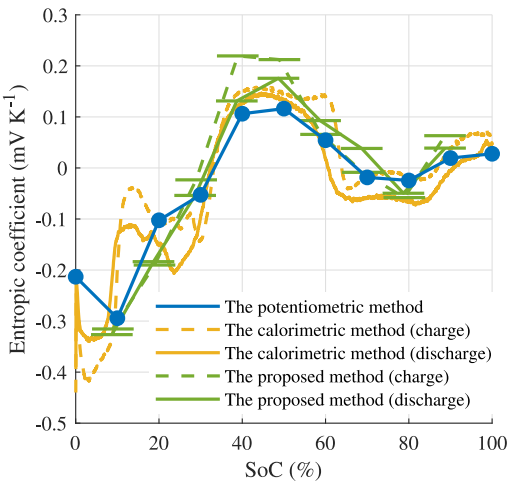

Figure 3.8: Summary of the entropic coefficient measured by the three methods: the potentiometric method, the calorimetric method and the proposed alternating current method.

The temperature coefficient of an electrode material can be measured with the potentiometric method and a symmetric H-cell setup [23], [24]. The configurational entropy can also be measured with a half-cell consisting of the

electrode material of interest and a lithium metal counter electrode. When it comes to commercial cells, the classic potentiometric method is time consuming due to the relatively large thermal capacitance of the cell. Moreover, the cell temperature has to be controlled with an external device, either a climate chamber or a resistive heater. To characterize the temperature coefficient of a commercial cell effectively, a new method was proposed in **Paper I** by applying alternating current on the cell. The fundamental component in the temperature response is clearly visible under 1C rate and can be used to calculate the temperature coefficient. The results have been experimentally verified with the potentiometric, as well as the calorimetric method, shown in Fig. 3.8.

3.4 Mechanical characterization

The lithiation and delithiation processes often lead to volume expansion and contraction of the electrode, illustrated in Fig. 3.9. The mechanical force introduced by this phenomenon can cause particle cracking and thus aging in Li-ion batteries [25]. Besides the reversible swelling during cycling, the volume of a sealed cell often increases with aging due to gas formation, which is irreversible. Understanding the mechanical characteristics is vital to design a suitable battery pack, so that the pack structure can endure the pressure increase and at the same time provide an optimal operation condition to prolong the battery lifetime.

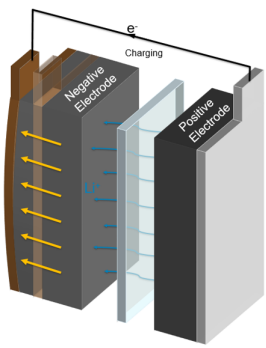

Figure 3.9: A schematic of volume expansion of a Li-ion cell during charging.

In this work, the reversible swelling phenomenon is studied in two scenarios, one with a constant volume and one with a constant pressure. The irreversible swelling is observed in both cases but not studied in details.

Pressure change during cycling with a fixed volume

In this setup, 4 compression load cells (TE FC2311-0000-0500-L) are used to measure the force at different locations on the battery cell surface. The schematic is shown in Fig. 3.10. Lock nuts are used to ensure a fixed thickness. The force on the battery cell is transferred to the load cell via a middle aluminium plate, which evens out the pressure applied on the cell. During the testing, the test setup is placed in a climate chamber under a constant temperature. Type K thermocouples are placed on each load cell, as well as on the Li-ion pouch cell. The battery cycler is the PEC ACT0550. The compression load cells are powered and measured with Ipetronik M-sens.

Four current levels (1 A, 12.5 A, 25 A, and 50 A) are applied on a 26 Ah pouch cell at three temperatures (5 ^{o}C, 20 ^{o}C, and 35 ^{o}C). The cycling protocol is constant current constant voltage until 0.01 A cut-off current, followed with a relaxation period of 10 hour, the same for charge and discharge. This ensures that each test starts from an equilibrium state. Each test case is repeated twice to check the measurement quality.

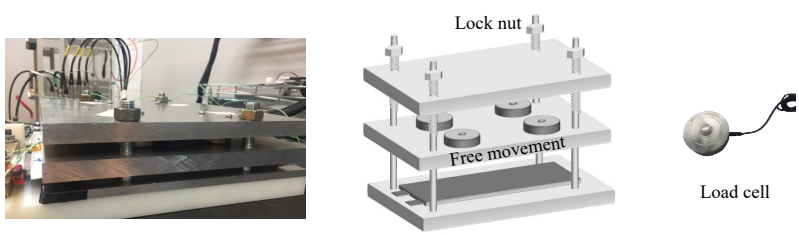

Figure 3.10: The setup design the implementation to measure the cell surface pressure with a fixed distance.

The pressure change ΔP under 1 A cycling at different temperatures are shown in Fig. 3.11. Up to 55 kPa pressure change can be detected during charging, when 60 kPa pressure is applied at 0% SOC at 5 ^{o}C. The repetitive

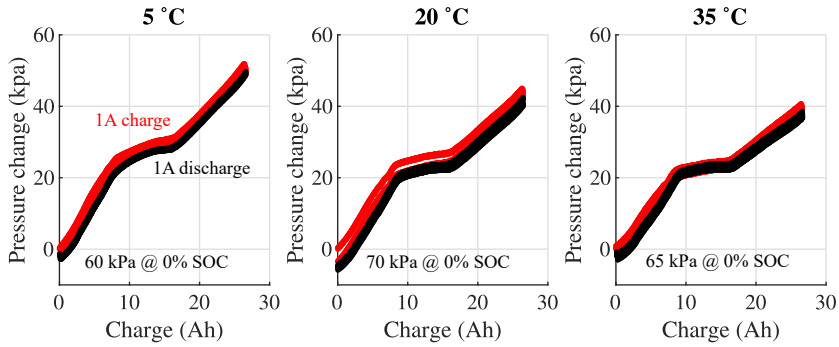

Figure 3.11: The cell pressure change under 1 A cycling at 5 ^oC, 20 ^oC and 35 ^oC.

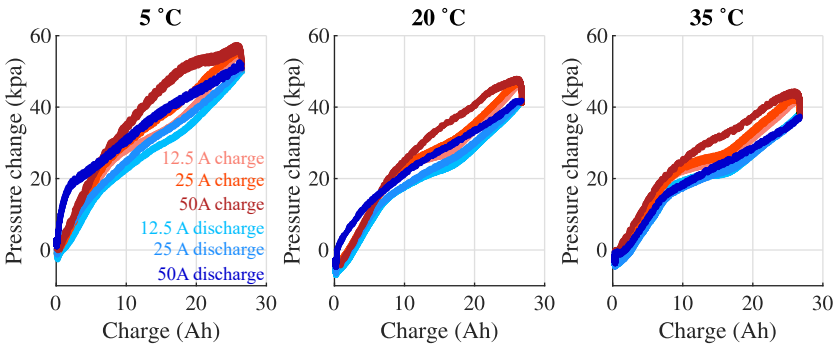

Figure 3.12: The cell pressure change under 12.5 A, 25 A, and 50 A cycling at 5 ^oC, 20 ^oC and 35 ^oC.

cycles are plotted as well and the overlapping indicates a reliable result. It can be observed that the pressure change is larger at a lower temperature. Moreover, a clear staging behaviour appears in all cases which is most likely related with the graphite electrode [26]. The offset pressure at 0% SOC differs slightly which can be related with the history as well as the temperature dependency of the compression load cell itself.

The results under higher current levels are presented in Fig. 3.12. A higher current will cause a larger overpotential which can be reflected in the pressure measurement. The impact of temperature is similar as what was shown in

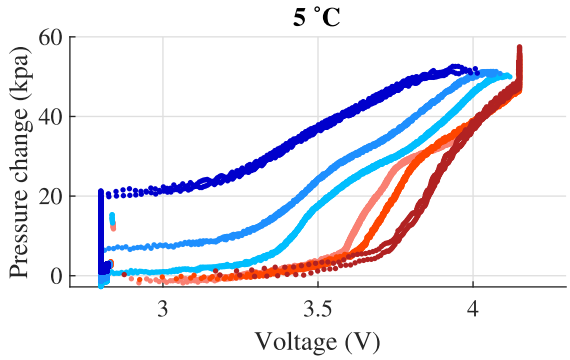

Figure 3.13: The cell pressure change under 12.5 A, 25 A, and 50 A (C/2, 1C and 2C) cycling at 5 ^oC plotted versus cell voltage.

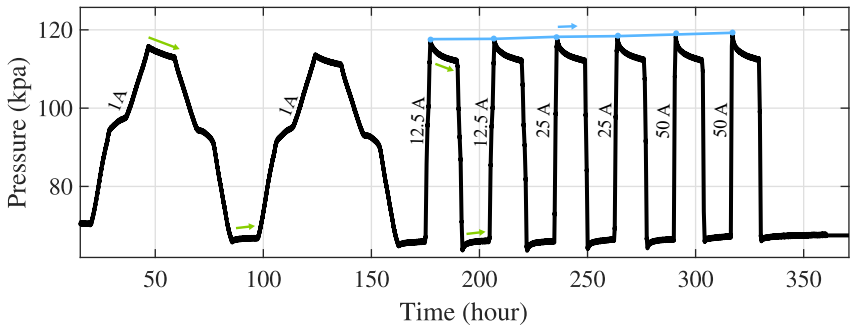

Figure 3.14: Pressure measurement time series at 20 ^oC.

the 1 A cycling. There is a crossing behaviour observed under 50 A cycling at both 5 ^oC and 20 ^oC, therefore an extra plot of pressure change versus cell voltage is provided in Fig. 3.13 where a clear trend can be noted.

In Fig. 3.12 at 50 A, 5 ^oC, the cell is charged under a constant current from 0 Ah to 16.6 Ah and then charged under a constant voltage, 4.15 V. However, after 23.5 Ah, there is a significant pressure increase taking place. This might indicate that a side reaction is happening, possibility lithium plating [27].

The pressure measurement for a time series at 20 ^oC is presented in Fig. 3.14.

The green arrows indicate the pressure change during the 10 hours relaxation period, which is related with the redistribution of Li-ions. Moreover, an increasing trend can be found based on the peak pressure in each cycle, indicating an irreversible cell swelling due to gas formation.

Volume change during cycling with a fixed pressure

The setup above with a fixed volume is often the case in real applications, however, in laboratory environment it is possible to allow the cell to swell freely and measure the volume change. In this setup, two laser sensors (Baumer OM70-L0070.HH0065) are used to measure the thickness change of the cell at two locations, one close to the tabs and the other away from the tabs, shown in Fig. 3.15. There is no external pressure applied on the cell except the atmosphere pressure. The battery cycler is PEC ACT0550. The laser sensors are powered with an external power supply and measured with Ipetronik M-sens. Three current levels, 2.5 A, 5 A and 25 A are applied to cycle the cell at room temperature.

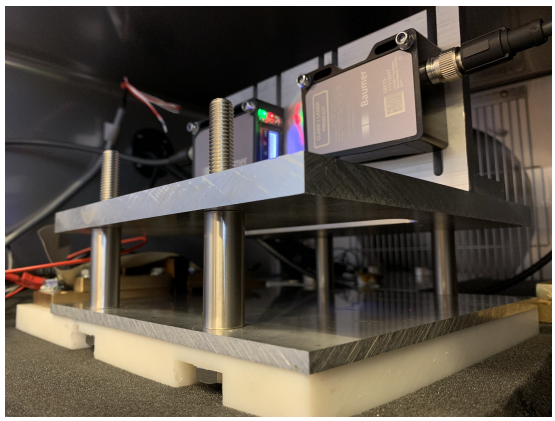

Figure 3.15: Experiment setup to measure the cell thickness change during cycling.

The measured thickness change of a Li-ion cell under different current levels are presented in Fig. 3.16. It can be observed that at the location close to the tabs (solid lines), the swelling is stronger since the current density is higher than at the location away from the tabs (dashed lines). The total thickness change is around 150 μm (2% of the cell thickness), and it is not affected by

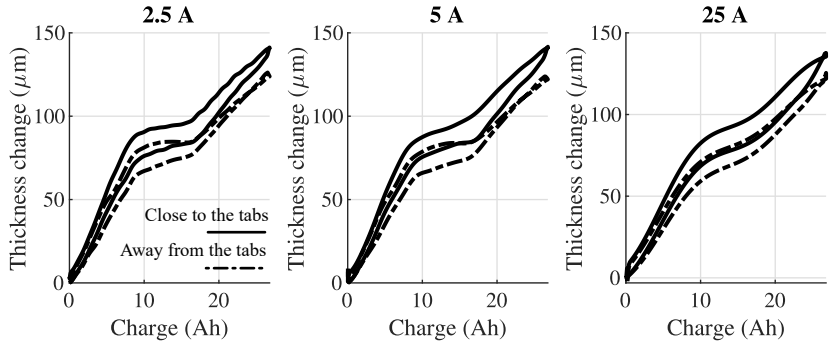

Figure 3.16: The cell thickness change during cycling at 2.5 A, 5 A, and 25 A (C/10, C/5, and 1C) at room temperature.

the current level significantly. A staging behaviour is observed, same as in the pressure measurement, which might be explained by the graphite staging property. A time series measurement is shown in Fig. 3.17. A clear increasing trend can be found, indicating an aging process.

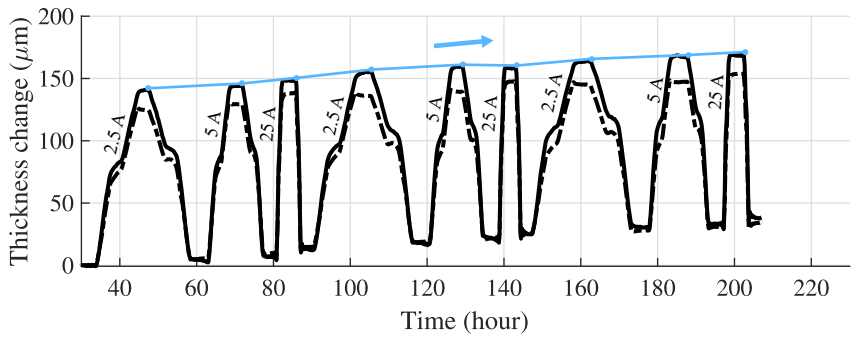

Figure 3.17: Thickness measurement in time series showing an increased volume trend with aging.

There have been attempts to measure the cell thickness change in a temperature swing without current but the results were inconclusive. In the latest

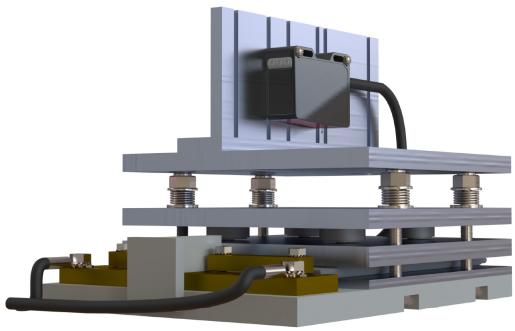

Figure 3.18: A combined setup to measure the cell thickness change and pressure in a spring loaded test jib. Credits to Gabriel Hassellöf for the drawing.

attempt, the cell tabs were not attached to the current cables and stainless steel tubes are used to hold the sensor brackets to reduce the metal formation during the temperature swing. In a future work, a plate with smooth surface could be employed to avoid the impact of the cell surface roughness.

Last but not least, it is possible to combine these two setups and measure the pressure and thickness change of the cell at the same time in a spring loaded test jig, shown in Fig. 3.18.

CHAPTER 4

Temperature swing setup

4.1 Test design to create different temperature swings

The thermal system of a test jig can be modelled with a first order system and the the mathematics description is

$$C\frac{dT_{cell}}{dt} = \frac{1}{R_{th}}(T_{cell} - T_{amb}) + Q_{cell} + Q_{add} \tag{4.1}$$

where C is the thermal capacitance of the system, t is time, R_{th} is the thermal resistance between the cell and ambient, and T_{cell} is the cell temperature, ignoring the temperature distribution within the cell in the system modelling. The total heat generation in the system comes both from the battery cell itself Q_{cell} and the additional heat source Q_{add}. In (4.1), T_{cell} is the output variable and other parameters can be controlled with different configurations. The target of this project is to demonstrate how the thermal stress, i.e. ΔT_{cell}, affects the battery lifetime. To realize this target, the following objectives are considered during the test design:

- The cycling current shall be the same for all cells to decouple the current impact on aging, meaning that Q_{cell} are very similar in all setups.
- During cycling, the cells shall have the same average temperature $T_{cell,avg}$, but with different temperature swings ΔT_{cell}.
- The ambient temperature T_{amb} of all cells shall be the same to be resource efficient so that only one climate chamber is needed for the long-term testing.
- Two cells shall be cycled in each thermal condition to check the repeatability.
- At least three different temperature swings shall be created.

As described above, T_{amb} and Q_{cell} are constants for all setups and the other parameters C, R_{th} and Q_{add} can be controlled to comply the objectives. It can be noted from (4.1) that a small thermal capacitance and large heat generation can create a high temperature swing, i.e. high thermal stress, with a magnitude of

$$\Delta T_{cell} = \frac{Q_{total}}{C} \tag{4.2}$$

On the other hand, the average temperature is decided by the thermal insulation and average heat generation,

$$T_{cell,avg} = R_{th} Q_{avg} \tag{4.3}$$

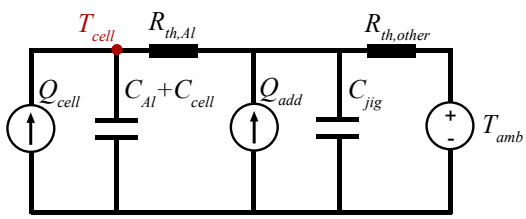

Figure 4.1: The lumped parameter network model for the thermal behaviour of the test jig system.

To check how the parameters in (4.1) affect the cell temperature, a lumped parameter network (LPN) model was implemented as shown in Fig 4.1. In the

simulation, two RC links are used to describe the system. The thermal resistance $R_{th,Al}$ represents a thin aluminium plate between the cell and heating source to ensure a more evenly distributed temperature. Before conducting any experiment, the parameters in the LPN model are roughly estimated as the following:

- $Q_{cell} = I^2 Z_{cell} = 7.5$ W, assuming $I = 50$ A (2C), $Z_{cell} = 3\text{m}\Omega$ (based on previous experiments), ignoring the temperature and SOC dependency of the cell impedance, as well as the entropic reversible heat. The input current design is shown in Fig. 4.2 to form a square wave shaped heat dissipation.

- $C_{cell} = 550$ J/K [28].

- $R_{th,Al} = d_{Al}/Ak = 0.001$ K/W, where the aluminium (Al) plate thickness $d_{Al} = 10$mm, plate area $A = 15\text{mm}\times 20\text{mm}$ and the thermal conductivity $k = 167$ K/(m·W). The thermal conductivity of pure Al is around 237 K/(m·W). However, in the real applications the plate is made of an aluminium alloy. The value 167 K/W is used as an estimation since the exact alloy compound is unknown in this case.

- Q_{add} is adjusted based on the need. To boost temperature swings in some of the tests, an additional heat is enabled when the cell current is applied and disabled when the cell is relaxing.

- C_{jig} consists of the contributions from the brass tab connector, Al and nylon plates in the setup in Fig. 4.4. The heat capacitance of each component is calculated as $C = C_s Vol \rho$, where C_s is the specific heat capacity, Vol is the volume of the component and ρ is the density. The brass pieces are the same in all setups and $C_{brass} = 319$ J/K. The rest of the system is configured by adjusting the thickness of the plates to obtain different C_{jig}.

- $R_{th,other}$ represents the thermal resistance due to heat conduction in the Al and nylon plates, calculated as $R_{th,cond} = d/Ak$, and the heat convection in the air, calculated as $R_{th,conv} = 1/hA$. The convection coefficient used in the model is 20 K/W·m^2 since there is a fan circulating the air in the climate chamber. The heat conduction through the current feed cables are not included in the model. Although the heat leakage

through the cables can be a significant part, it is considered better to exclude it and have a clean model rather than using values without a good base.

- $T_{amb} = 20^{o}$C, controlled by the climate chamber.

The input current is designed as shown in Fig. 4.2. The 30 minutes idle time is to allow the battery to cool down so a temperature swing can be created. With the configuration in Table 4.1, the simulated temperature profile is shown in Fig. 4.3. The result is as expected, a high power, small heat capacitance (inertia) with a low thermal insulation can create a high temperature swing. During the first few cycles, the average heat dissipation elevate the average temperature and after 15 hours all setups reaches the same average temperature. When it is time to perform the RPT, the cell is cooled with natural convection to the ambient temperature which is set to be 20^{o}C. This guarantees that the characterization of all cells are performed at the same temperature to make a fair comparison.

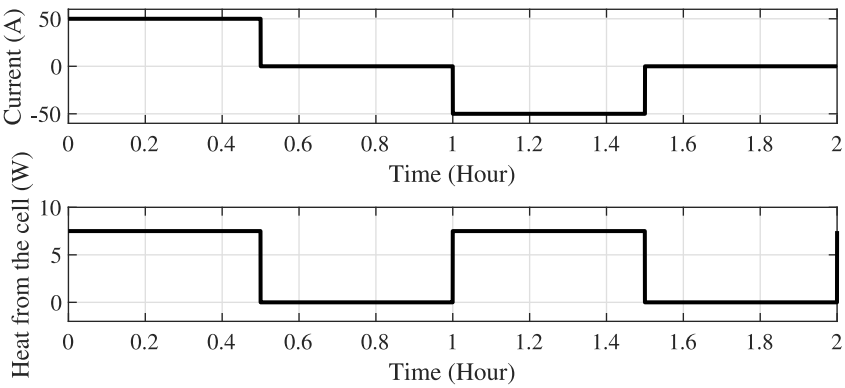

Figure 4.2: The designed current input during cycling and the estimated heat dissipation from the cell assuming the cell impedance is 3 mΩ.

The simulation proves the feasibility of the design idea and provids a guideline for the real implementation. In reality, the thermal insulation and additional heat source were tuned based on trial and error to create the desired

Table 4.1: Test jig design used in simulations to create different temperature swing (TS) cases

Case	Q_{add} [W]	C_{jig} [J/K]	R_{th} [K/W]
High TS	17.5 W	866	0.4
Medium TS	2.2 W	1960	1.0
Low TS	0	6338	1.26

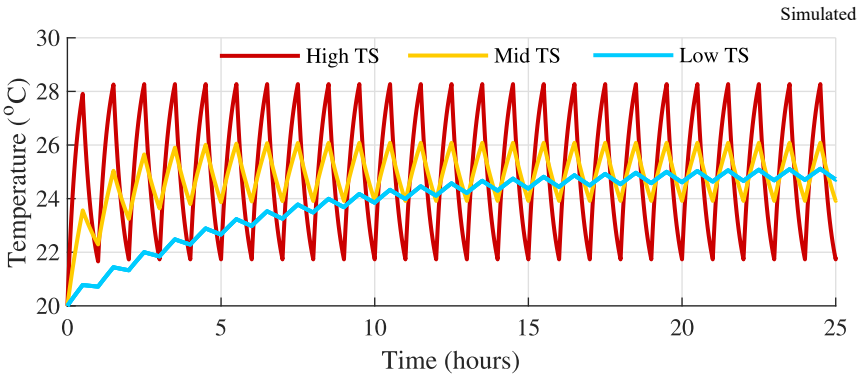

Figure 4.3: The simulated temperature swing using the lumped parameter network model described in Fig. 4.1.

temperature pattern. Therefore the actual values of R_{th} and C_{jig} in the system differs from what was estimated in Table 4.1. The final implementation of the test jig is shown in Fig. 4.4. An in-house designed cover is used in the mid and low TS case which was manufactured with 3D printing and a vacuum machine. The additional heat power in the final implementation is 22 V×1.4 A = 30.8 W for the high TS case away from the cooling fan, and 24 V×1.5 A = 36 W for the high TS case close to the fan (this will be further explained in the test matrix section). The mid TS case has an extra heat of 10.6 V×1.35 A = 14.3 W and there is no extra heat for the low TS cases. One example of the measured temperature swings is shown in Fig. 4.5, which matches the expectation as it approximately resembles the simulation results in Fig. 4.3. The temperature peak during discharge is higher due to the high impedance at low SOC, and also due to the entropy effect.

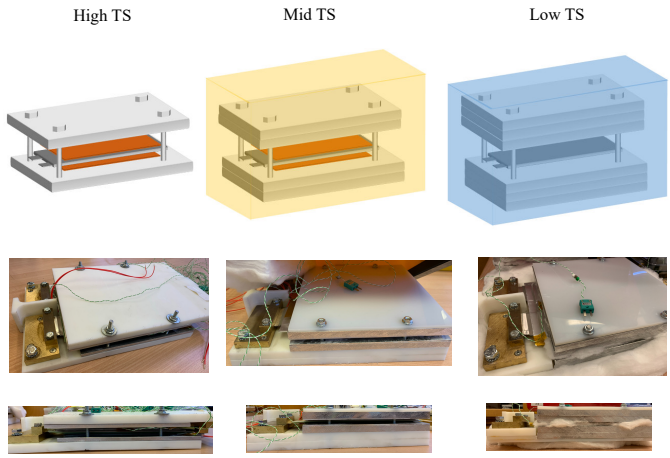

Figure 4.4: Implementation of the setup to create different temperature swings.

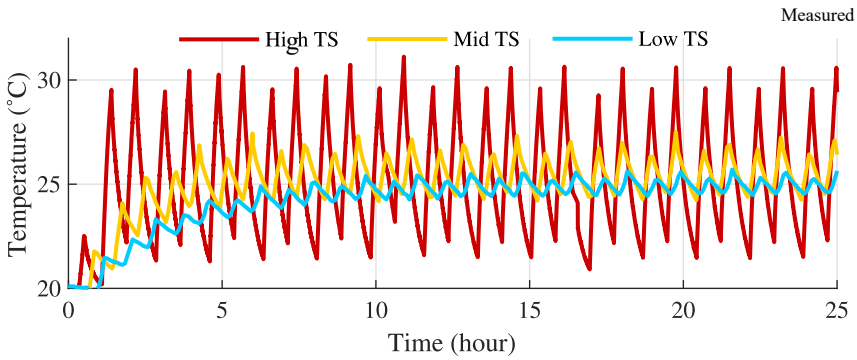

Figure 4.5: The measured temperature swing

4.2 Test matrix and equipment

In total 12 cells from the same batch are used in the aging setup, described in Table 4.2 and Fig. 4.6. Cell A1 and A2 have standard jig setups where the

aluminium plates are used to apply a certain pressure on the cell to mimic the condition in a battery pack. Cell B1 and C1 are clamped in the same jig, shown in Fig. 4.6 so that Cell B1 experiences the same temperature as C1 but without current. Two resistive heaters are used on both sides of the cell to reduce the uneven temperature distribution across the cell. All cells are located in one climate chamber and hence the cell located close to the cooling fan has a lower temperature compared to the cell located close to the door. The additional heat for the cell close to the fan is tuned higher to compensate the uneven air temperature distribution within the chamber.

Table 4.2: Test matrix with different temperature swings

Cell	Cycling current	Voltage	TS	RPT	Comment
A1	0	3.05 V	T_{amb} constant	Sync with C1	Calendar aging
A2	0	2.8 V-4.15 V	T_{amb} constant	Continuously	Aging caused by RPT
B1	0	3.05 V	Same as C1	Sync with C1	Aging caused by TS
B2	0	3.05 V	Same as C2	Sync with C2	Replicate of B1
C1	+2C/-2C	3 V - 4V	High swing	Scheduled	
C2	+2C/-2C	3 V - 4V	High swing	Scheduled	Replicate of C1
D1	+2C/-2C	3 V - 4V	Mid swing	Scheduled	
D2	+2C/-2C	3 V - 4V	Mid swing	Scheduled	Replicate of D1
E1	+2C/-2C	3 V - 4V	Low swing	Scheduled	
E2	+2C/-2C	3 V - 4V	Low swing	Scheduled	Replicate of E1

During the aging test, the cells are cycled with a battery tester PEC ACT0550 with a 4-wire connection. Each channel is equipped with one PT100 temperature sensor. Besides, type K thermocouples are used to measure the temperature at the other locations of interest. The specification of the equipment is listed in Table A.1. The cells being cycling aged, are cycled within a limited voltage window between 3 V and 4 V, to avoid specific aging mechanisms that are associated with the highest and lowest SOC. The battery degradation processes are more complicated at those SOC levels and therefore they are not targeted in this work.

The heaters are turned on at the same time when the current is on. This is achieved by using the digital output (DO) module in the PEC auxiliary input and output system (AIOS). Right before the current is applied on the cell, the tester will send out a signal via CAN to enable the DO module to turn on the heater, illustrated in Fig. 4.7a. This is possible since both the current and voltage of the heater are within the limits of the DO module.

The AIOS is also used to synchronise the RPT schedule between Cell A1

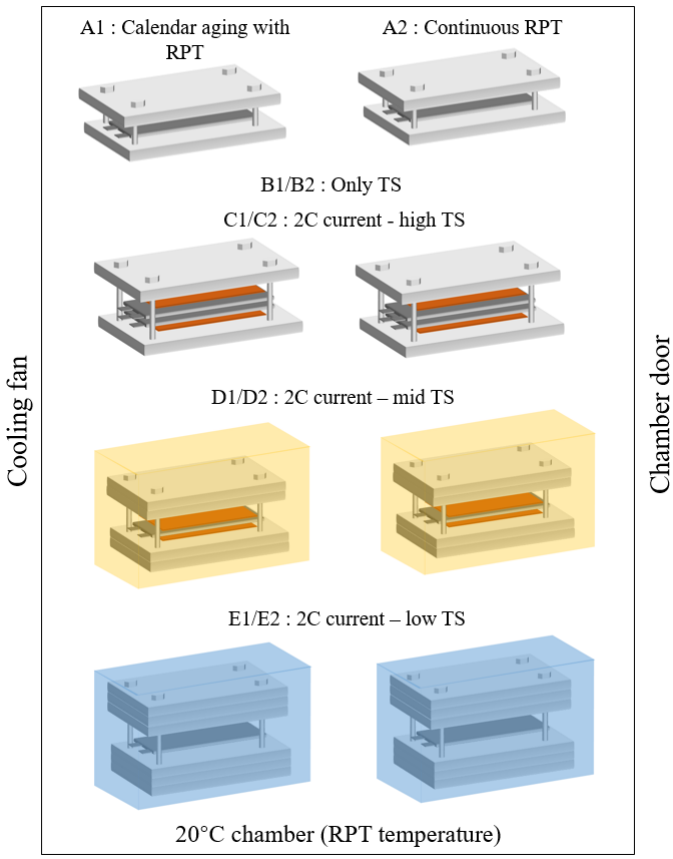

Figure 4.6: The layout of the cells inside the climate chamber.

and C1. When it is time to perform the RPT for C1, the channel connected to Cell C1 will send out a CAN signal to enable a DO module, which is physically connected to an analog input (AI) module. At the same time, the channel for Cell A1 is constantly checking the signal received from the AI module. As soon as the signal is received, the channel will perform an RPT on Cell A1, illustrated in Fig. 4.7b. The same principle applies to the synchronization between Cell B1 and C1, and between Cell B2 and C2.

Also, some practical actions were made: Thermal paste is used between

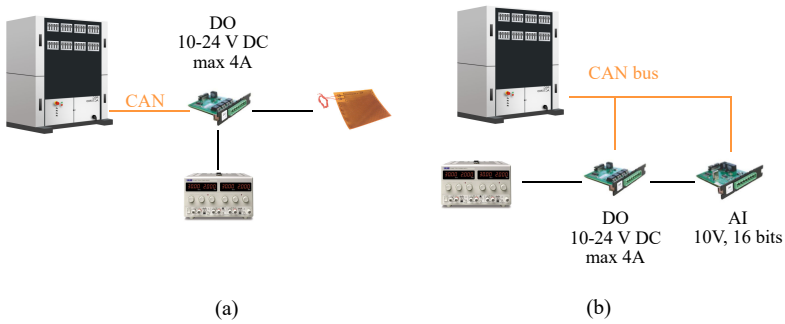

Figure 4.7: Setup of the AIOS.

cells, heating mats and aluminium plates, to reduce the thermal contact resistance caused by the air gap and achieve an even temperature distribution. When placing the cells in the test jig, a torque wrench is used to tighten the screws, so that the applied pressure is similar in all test jigs, although the absolute pressure is not measured. For the low thermal stress case, cotton is used to fill all the air gaps around the jig to reduce the natural air convection, and thus increase the corresponding thermal resistance.

4.3 Reference performance test

The RPT is designed as shown in Fig. 4.8, including a 1C capacity test, ICI test (described in **Paper III**), 1 kHz resistance and EIS measurements (at 2.8 V, 3.7 V, and 4.15 V), 2C charge pulses (at 2.8 V and 3.7 V), and 2C discharge pulses (at 4.15 V and 3.7 V).

The cycler PEC ACT0550 used in this work does not provide an integrated EIS solution, but luckily it supports the drive cycle operation mode with maximum 1 kHz update rate, which makes it possible to perform an in-situ EIS measurement within a limited frequency range up to 100 Hz. One example of a 100 Hz sine wave with 3 A peak current and its voltage response are shown in Fig. 4.9. To be noted that the cycler takes around 1 ms to switch the current sign and this 1 ms blank time during switching can introduce a significant distortion at high frequencies. Because of this feature, a DC current (25 A is

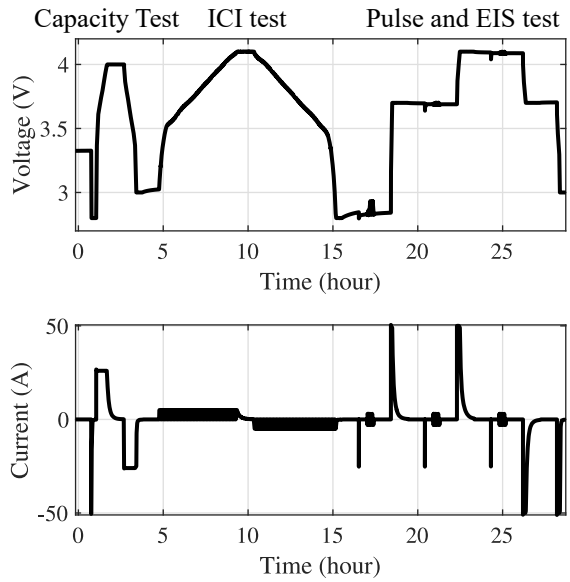

Figure 4.8: The RPT sequence used in the aging test, including a 1C capacity test, ICI test, 1 kHz AC impedance tests, EIS tests and pulse tests.

used in this work) is required during the 1 kHz AC impedance measurement to obtain an accurate result.

In this in-situ EIS measurement, a series of sinusoidal waves from 100 Hz to 2 mHz are generated from MATLAB in advance and fed as a drive cycle in the cycler. The sine waves are repeated 5 cycles at high frequencies to reduce the impact of noise and distortion, and 2 cycles at low frequencies (below 10 mHz) to reduce the test time. The sampling speed is 1 kHz at high frequencies to acquire a sufficient amount date, and 10 Hz at low frequencies to not overload the CAN bus. If the bus is overloaded, the test will be paused until all the data in the buffer are transmitted, which can introduce disturbances in the EIS measurements.

Beside the EIS measurement, the battery resistance is also tracked with

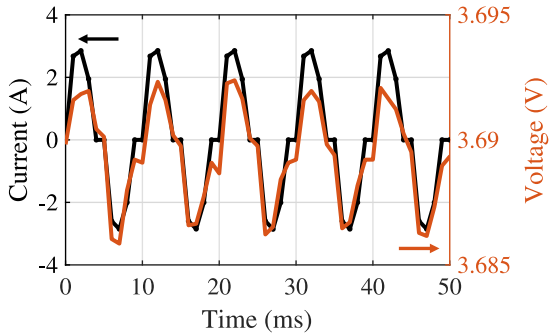

Figure 4.9: A 100 Hz sine wave with 1 kHz update rate to measure the cell impedance.

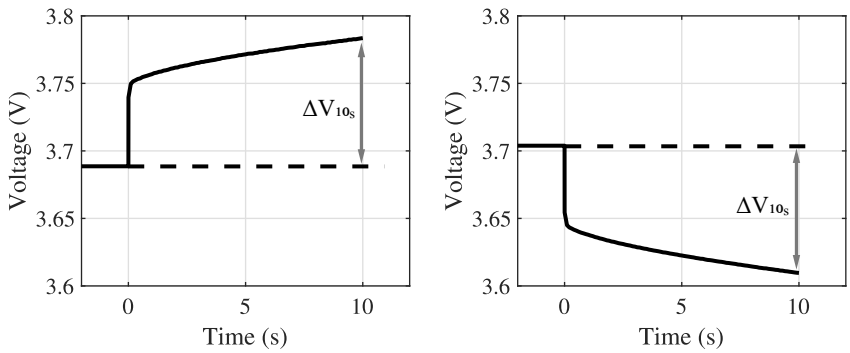

Figure 4.10: The voltage responses during 2C charge (left) and discharge (right) pulses.

high power pulse tests. The 2C pulse resistance is calculated as

$$R_{10s} = \frac{\Delta V_{10s}}{I} \tag{4.4}$$

and the voltage change ΔV_{10s} is between the equilibrium voltage and voltage response after 10s, illustrated in Fig. 4.10. The high power pulse resistance is a total product including the impedance of different electrochemical processes,

as well as the change in the open circuit potential, and it can better reflect the battery power capability. In an earlier study in Fig. 1.1, it was found that, for the cell used in this work, the discharge resistance is higher than the charge resistance. Therefore, charge and discharge pulses are applied at the same voltage to study the impact of the current sign on the resistance value.

4.4 Temperature distribution and contact resistance

It is believed that the high TS cases (Cell C1 and C2) will have the most uneven temperature distribution, which is interesting to monitor. However in most of the cases it is not easy to access the temperature at the center of a pouch cell surface when the cell is placed in the holder. In the test jig of Cell C1, the inner Al plate is specially manufactured with a 2 mm slot milled, so that a type K thermocouple can be inserted in the middle of the pouch cell without introducing uneven pressure on the surface, as shown in Fig. 4.11a.

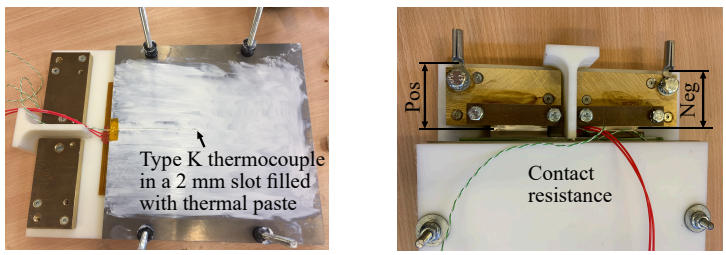

Figure 4.11: Setup to measure (a) the temperature at the center of the cell. (b) the contact resistance on the tabs.

Another concern is that the electric contact resistance between the battery tab and current carrying cables can cause extra heat dissipation and the contact resistance might increase with time due to metal corrosion and deformation. In the laboratory environments, the battery tabs are generally placed between two brass pieces and clamped with screws. It is challenging to achieve a good contact in such a setup without welding the tabs permanently. In an

earlier attempt, a rough surface with pyramid shapes on the brass pieces are employed to have secured contact points. In this work, flat brass pieces are used with copper paste applied between the cell tabs and current connections to reduce the contact resistance, and thus reduce the heat generation in the connections. The voltage drop across the contact is measured through the entire experiment, shown in Fig. 4.11b.

CHAPTER 5

Temperature swing results

5.1 Capacity fading with aging

The aging test started in August 2019 and was terminated in November 2021. Some cells have been stopped earlier due to errors in the connectors. Power interruptions occurred multiple times in the lab but it is considered that the interruptions did not affect the results significantly. The cells have only been cycled between 3 V and 4 V, to avoid the aging processes at the highest and lowest SOC levels. Besides the limited voltage window that is utilized, the cells are exposed to a relatively mild temperature conditions. The resting period between each charging and discharging is 30 minutes (Fig. 4.2). These factors likely lead to a much longer lifetime of the cells [29]. Therefore not all the cells reached their end of life after two years. In this case, the end of life is defined when the a cell reached 80% of its initial capacity.

In Fig. 5.1, the capacity degradation of the cells being both current and temperature cycled are presented. The CCCV capacity describes the cyclable lithium inventory, while another more commonly used capacity, the 1C discharge capacity, is determined both by the CCCV capacity and the cell impedance and therefore lower than the CCCV capacity. The dashed lines

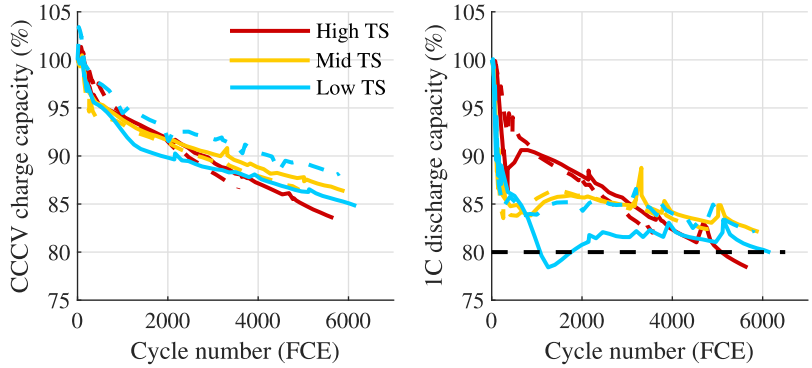

Figure 5.1: Capacity fading with cycling aging. The dashed line for the replicate test case.

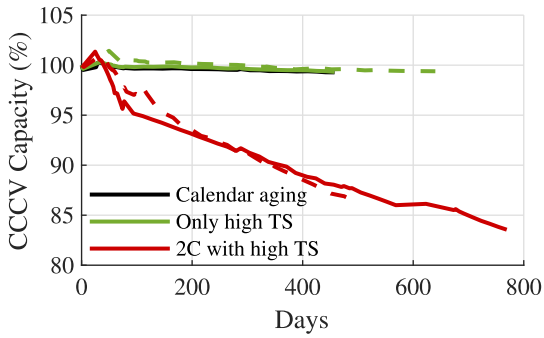

Figure 5.2: Capacity fading with calendar aging (black line), pure temperature cycling aging (solid and dashed green lines). The capacity fading of 2C high temperature swing aging case are plotted as references (solid and dashed red lines). The green lines overlap with the black line.

refer to the replicate cells. It can be noted that the cells with a high temperature swing have a moderate aging trend in the beginning, but then degraded faster in the later cycles. The difference between the three cases are not dramatic since the test conditions in general were not extreme. For the high

and mid temperature swing cases, the aging trends are consistent between the two replicate cells. One of the cells exposed to a low temperature swing shows a similar aging trend as the mid temperature swing case. However, the other cell degraded quickly to its end of life but recovered with the cycling afterwards. No obvious evidence has been found to explain this observation.

The capacity fading of the other cells are presented in Fig. 5.2. The cells being only temperature cycled show the same trend as the calendar aged cell, indicating that a pure temperature cycle between 20 ^oC and 30 ^oC does not introduce a notable aging effect to a Li-ion cell.

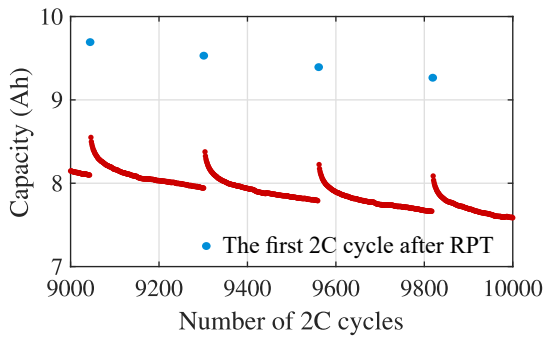

Figure 5.3: 2C capacity of Cell C1 during cycling. The voltage window is between 3V and 4V.

A clear capacity recovery behaviour can be observed in the 2C capacity determined in the voltage window between 3V and 4V, shown in Fig. 5.3. This capacity recovery occurs after an RPT is performed, which is similar as a "resting" period as the characterization current during the RPT is lower than the 2C cycling current. This capacity recovery behaviour has been explained with charge redistribution in the anode overhang area [30] if the cell is left resting at a low SOC, or a self-enforcing process of lithium plating [29]. Based on the relaxation voltage when the 2C current stops at the high SOC, no significant lithium plating is observed in the cell used in this work. Therefore the capacity recovery observed here is more likely related with the anode overhang effect.

5.2 Incremental capacity analysis (ICA) and differential voltage analysis (DVA)

The incremental capacity analysis (ICA) and differential voltage analysis (DVA) are two methods that are commonly used to track the battery degradation. Often, the voltage response under a constant current is used to perform the analysis. In this work, the voltage response from the ICI test (C/10) during RPTs are used, which can provide equivalent information as a constant current test, despite the short interruptions and the validity was analysed in **Paper III**.

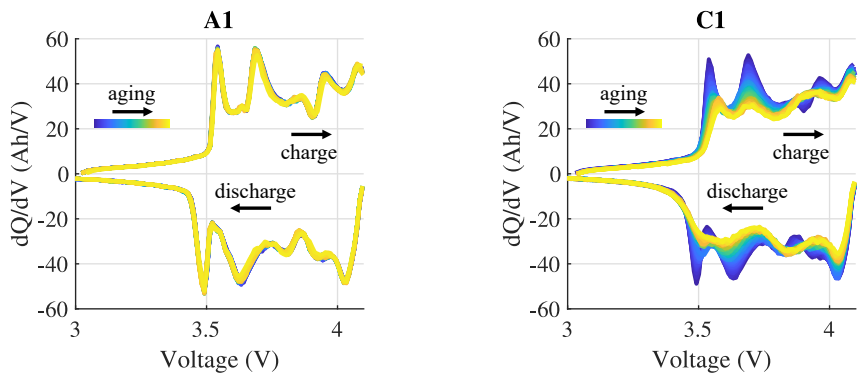

Figure 5.4: The incremental capacity analysis curves change with cell aging.

In Fig. 5.4 and Fig. 5.5, the ICA and DVA curves of Cell A1 and C1 are shown. These two representative cases are selected since Cell A1 is the least aged cell while Cell C1 is the most aged cell. The peaks in the ICA curve correspond to a certain phase in the electrode material, which was analysed in Fig. 3.8 from [4]. It can be noted that Cell A1, which was only under calendar ageing, does not show an obvious degradation. On the other hand, the reduction in the peak heights and the shift of the peak locations in the ICA curves of Cell C1 indicating a significant capacity degradation and resistance increase. The degradation of Cell C1 is stronger in the middle range of the voltage window, which is reasonable since the cell has been mainly cycled between 3 V and 4 V. The peaks in this range are mainly related with the graphite and the NMC in the positive electrode. The peaks related with the

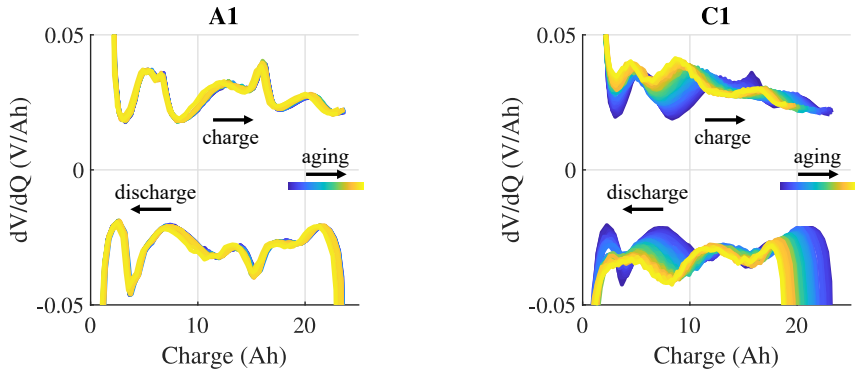

Figure 5.5: The differential voltage analysis curves change with cell aging.

LMO are located at the higher potentials which are less affected. The curves of other cells are presented in the Appendix Fig. B.1 and Fig. B.2.

There is a minor shift of the peak locations between charge and discharge, caused by the cell impedance. To reveal the cell characters more clearly, a lower current C/20 is used to charge the cells after the aging test is finished. The resulting ICA and DVA plots are presented in Fig. 5.6 and Fig. 5.7. The results are consistent with the capacity fading trend, that a pure temperature cycling does not age the cell. Moreover, the peak heights of the cell cycled with 2C current and high TS, are heavily reduced, indicating a severe loss of the lithium ion inventory.

5.3 Resistance change with aging

ICI regression resistance and diffusive resistance

Besides the ICA and DVA curves, three more parameters are extracted from the ICI tests. The parameter extraction is demonstrated in Fig. 3.6 and the results are presented in Fig. 5.8. The ICI results of the other cells can be found in Appendix Fig. B.3, Fig. B.4 ,and Fig. B.5. R_0 is calculated based on the instant voltage change (2 ms) after the current interruption. This value can be related with the R_0 in the EIS measurement marked in Fig. 3.1. From the results, it can be noted that there is little change in the R_0 values for both

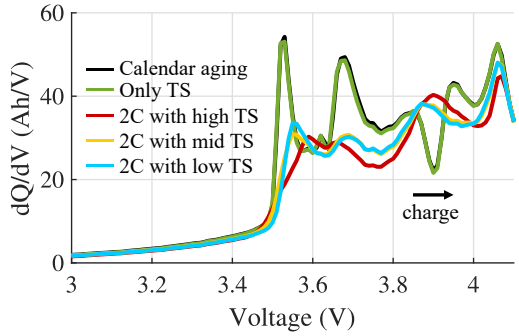

Figure 5.6: The incremental capacity analysis at the end of the cycles.

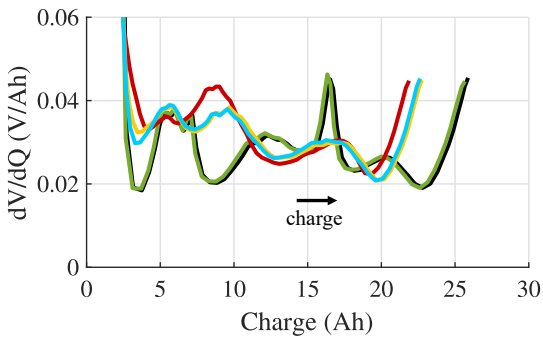

Figure 5.7: The differential voltage analysis at the end of the cycles. The legend is the same as in Fig. 5.6.

Cell A1 and C1, indicating that there might not be significant electrolyte degradation and current collector corrosion. The other two parameters, R_{reg} and k, are obtained based on the linear fitting of the voltage response versus the square root of time, $\sqrt{t}$, during the current interruption. In the results of Cell A1, there is little change in R_{reg} and k, which is expected as Cell A1 has only been calendar aged at 20 ^oC and 3V. On the other hand, the R_{reg} and k values are increasing continuously during aging for Cell C1, especially at the lower SOC range. The SOC dependency in R_{reg} can be explained by the

concentration dependent exchange current density. The k change with SOC is the result of two factors: a SOC dependent diffusion coefficient and the shape change of the OCV curve. The latter one was discussed in **Paper IV**.

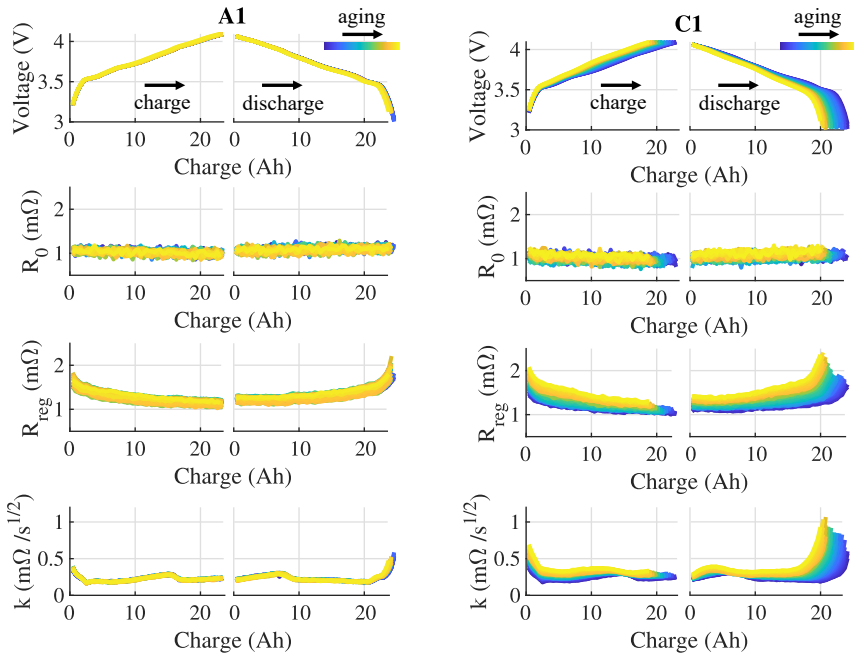

Figure 5.8: The ICI regression resistance R_{reg} and diffusive resistance k change with aging.

EIS

The EIS measurement results of Cell C1 at 3.7 V are presented in Fig. 5.9, based on the procedure described in Section 4.3. The other EIS measurement results can be found in Appendix Fig. B.6, Fig. B.7, and Fig. B.8. A Randles circuit is used to fit the date to provide a more clear trend. The fitted resistive and diffusive parameters from the Randles circuit can be related with the ICI parameters, which was discussed in **Paper III**.

Typically a frequency range down to 10 mHz is used to keep the cell in its equilibrium state during the measurement. In the even lower frequency range,

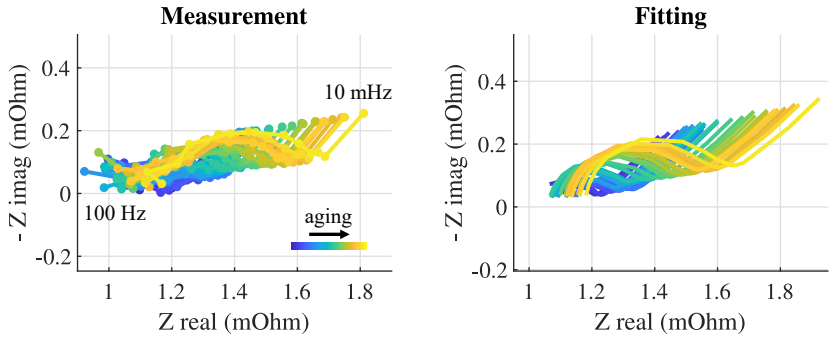

Figure 5.9: The EIS measurement during RPTs of Cell C1 at 3.7 V, and the fitted results based on a Randles circuit.

the cell SOC is moving during the EIS measurement and the corresponding voltage change starts to influence the impedance result. In this work, the impedance is measured down to 2 mHz and the impact of the voltage change during the measurement is analysed below. During the RPT, a C/10 ICI test is performed next to the EIS measurement, where a SOH dependent OCV look up table can be obtained based on the average between the charge and discharge curves. The OCV change during the EIS measurement can thus be calculated with coulomb counting and the look up table, which is plotted as the dashed line in Fig. 5.10. With a 3 A (peak value) 2 mHZ sine current wave, the terminal voltage change is up to 20 mV, among which the OCV change contributes 3 mV. The EIS results with and without the OCV change are shown in Fig. 5.11. A 45 degree line is marked as a reference, which is the phase of an ideal Warburg element. The impact of the OCV change can be ignored when the frequency is higher than 10 mHz. At a lower frequency, the over-estimation in the cell impedance becomes notable.

After the aging test is finished, a potentiostat GAMRY reference 3000 is used to measure the cell impedance at 3.7 V, shown in Fig. 5.12. It can be noted that the R_0 values are similar for all cells, while R_{ct} increases mainly with the current cycling, not the temperature cycling. The R_{ct} increase can be interpreted as an indicator of the surface film increase or reduced active surface area.

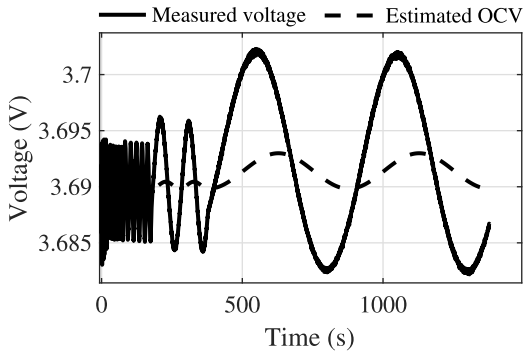

Figure 5.10: The estimated open circuit voltage change during the EIS measurement. Measured with Cell C1 at 3.7 V.

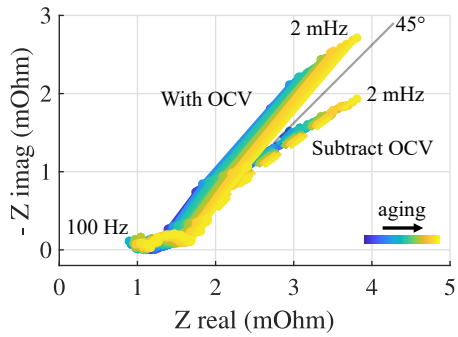

Figure 5.11: The EIS measurement with and without the OCV change. Measured with Cell C1 at 3.7 V.

2C pulse resistance

Based on the description in Fig. 4.10, the 10 second 2C pulse resistance of Cell A1 and C1 are presented in Fig. 5.13. The results for the other cells can be found in Appendix Fig. B.9. For cell A1, the pulse resistance keeps relatively constant throughout the aging test. The initial resistance decrease is often observed in literature, and it is possibly related with an increased

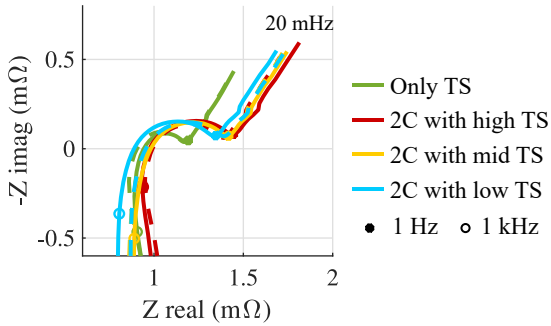

Figure 5.12: EIS measurement results at the end of the cycles with a potentiostat GAMRY Reference 3000. The dashed lines are for the replicate cells.

surface area during the initial cycles, which can be considered as a formation process [31]. The resistance increase in Cell C1 is pronounced, and in line with the observations from other characterization methods. The discharge resistance is slightly higher than the charge resistance, however the difference is very small.

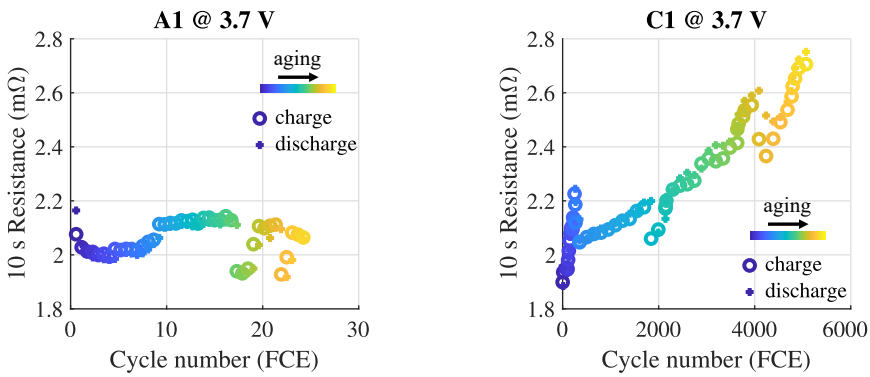

Figure 5.13: The 10 second 2C pulse resistance change with cell aging.

1 kHz resistance

The cycling equipment PEC ACT0550 has an in-build function to measure the 1 kHz AC impedance of the cell. The measured results are shown in Fig. 5.14. Increasing trends can be observed in all cases and the cells with high temperature swing have a slightly higher increase in the impedance. However, as marked in Fig. 5.12, the cell shows an inductive behaviour at 1 kHz and the resistance values at this frequency thus provides less information about the electrochemical properties of the cells [32].

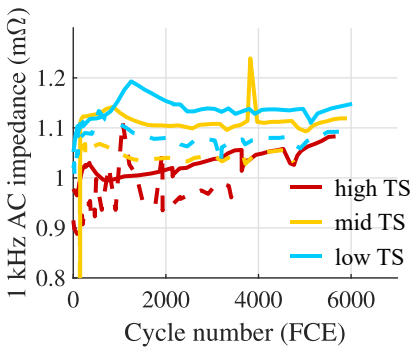

Figure 5.14: The 1 kHz AC impedance of the cells.

5.4 Temperature distribution and contact resistance

The temperature distribution around Cell C1 is shown in Fig. 5.15, both at the beginning of the cycles and at the end of the cycles. The temperature at the center of the cell surface is measured with the setup in Fig. 4.11a and the rest are measured with sensors attached from the side of the jigs. It can be noted that the center of the cell has the highest temperature and it is around 5 ^oC higher than the temperature at the gas pocket. The temperature inside the cell is expected to be even higher. In the beginning of the cycle, the cycling speed is 3 cycles per 0.2 days. With passing time, the cycling speed increased to be 4 cycles per 0.2 days, as the cell capacity decreases. Comparing the temperature

swing at Day 2 and Day 755, the overall temperature decreased, as a result of the reduction in the ambient temperature. This was likely caused by the ice formation in the chamber with the condensation water, which affected the temperature control of the system.

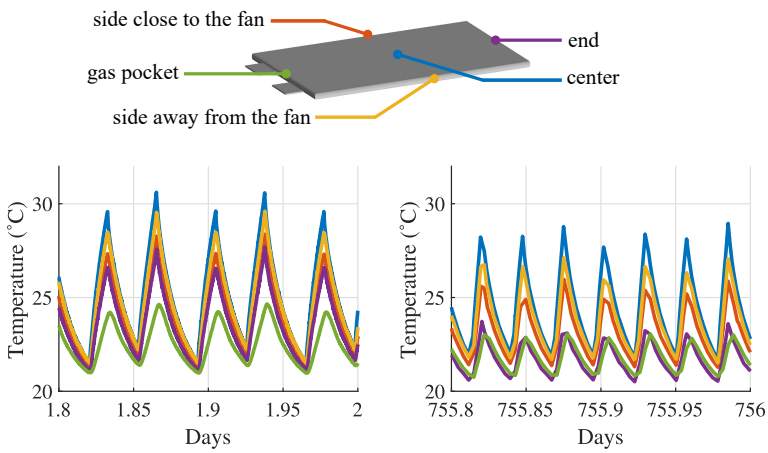

Figure 5.15: The temperature distribution around Cell C1 (high TS case).

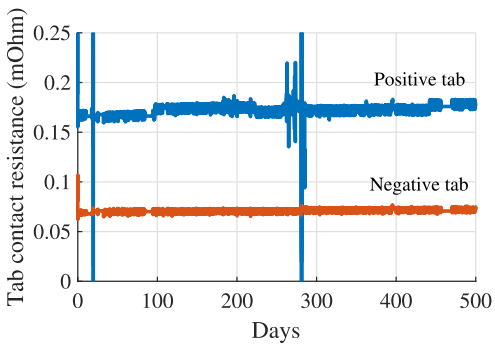

Figure 5.16: The contact resistance between the battery tab to the cable shoes on the current cable.

The contact resistance on the tab connections (Fig. 4.11b) are monitored through the entire test. The results in Fig. 5.16 show that the resistance at the positive side is higher than on the negative side, which is possibly due to the oxidation layer on the aluminium tab and the air gap created during the metal deformation. The positive contact resistance increased from 0.17 mΩ to 0.18 mΩ (6%) over 500 days and the negative contact resistance is more stable, with an increase from 0.069 mΩ to 0.073 mΩ (4%). This is considered to be a stable setup and the resistance value is much lower than the impedance of the battery cell and therefore the heat generation from the contact resistance can be ignored.

CHAPTER 6

Conclusions and future work

In this study, an experimental setup was developed to create different temperature swings on the battery cells with the same current magnitude, to examine how temperature swings affect battery lifetime. Based on the data of a 2 years aging test, the results show that the cells cycled under higher temperature swings aged faster. When the cell has been only temperature cycled without current, the aging behaviour is similar as a calendar aged cell without exposure to temperature swings.

A series of characterization methods were combined in the reference performance test to track the battery electrical characteristics during aging, including a 1C constant current cycle, a C/10 ICI test, 1 kHz AC impedance measurements, in-situ EIS measurements, and 2C pulse tests. The outcomes from different tests are highly consistent. Among these characterization methods, the ICI test is the most effective one. It can provide resistive and diffusive parameters in the whole SOC range throughout the battery lifetime, which are equivalent information as what can be extracted from the EIS measurement. Moreover, the ICA and DVA curves can also be generated from the ICI data.

Additional measurements were configured in the aging setup. The temperature sensor located in the middle of the pouch cell surface reveals that

the temperature gradient is 5 degrees across the surface during a 2C cycle. The temperature gradient is expected to be even higher if the cell internal temperature is considered, which is however not measurable in a commercial cell. The contact resistance between the battery tabs and the current cables were monitored through the entire test. This value is higher on the positive tab, possibly due to the oxidation layer and metal deformation of the positive aluminium tab. For 500 days, the contact resistance was stable, with only a 4-6% increase.

If a second test round would be possible, a higher magnitude of temperature swing can be applied as Li-ion batteries can operate in a much wider temperature range than what was used in this work, 20-30 ^{o}C. Moreover, more tracking methods can be added in the aging test, for example the pressure measurement and differential temperature voltammetry (the sampling speed of the temperature signal shall be increased). With multi-aspect diagnostic methods, it might be possible to distinguish the aging in each electrode, to some extent. Regarding the test design, the schedule of the RPT can be reduced. It was originally designed to perform an RPT when the 2C capacity decreases by 1 Ah compared with the 2C capacity after the previous RPT. However, the capacity recovery phenomenon was not considered which resulted in a too frequent RPT schedule. To extend the study, the temperature swing of a battery during usage shall be analysed in different applications, so that the aging test in the lab can be designed according to the application to better predict the battery lifetime.

Besides the aging test, which is the main part of the thesis work, several other activities were conducted and published. The additional conclusions are:

- The entropic coefficient of a large commercial cell can be effectively measured by applying a 1C square wave current. The obtained result agrees with what was obtained by the classic potentiometric method and also the calorimetric method.

- The transmission line structure is a bridge between the physics-based electrochemical model and equivalent circuit mode. The MATLAB based model provides a clear visualization of the electrochemical pro-

cesses in Li-ion batteries and the result is validated against COMSOL Multiphysics with less than 0.05% deviation.

- The ICI method is very useful when tracking Li-ion cell battery aging. It has relatively low requirements on the hardware regarding the sensor accuracy and sampling speed, and thus has the potential to be implemented in a battery pack with on-board equipment for aging diagnostics.
- The validity of GITT and ICI was examined with a black-box approach, when they are used to measure the Li^+ solid-state diffusion coefficient D_S in Li-ion batteries. Both of the methods can provide reasonable good results and the ICI is much more effective. The obtained D_s value is affected by the electrode potential profile, current distribution, charge transfer overpotential, as well as electrolyte mass transfer overpotential.
- The DC current on the battery pack of an electrified vehicle contains sufficient harmonics during driving, which can be used as the identification signal to measure the battery impedance in a frequency range between 0.01 Hz and 5 Hz. A signature value $R_0 + R_{ct}$ from the EIS diagram can be obtained with only CAN signals, which can be a useful information for aging diagnostic. The results were validated with lab experiments.
- The intercalation introduced reversible swelling, and aging introduced irreversible swelling of a Li-ion pouch cell, can be clearly observed via either pressure measurement or thickness measurement. The phase change in the electrode materials can be noticed in the measurements.

If time allows, the following continuation works would be very interesting. On the modelling side, it might be possible to bridge the physics-based electrochemical model and equivalent circuit mode even closer, by finding a physical interpretation of the RC link parameters. Another investigation would be the validity of the EIS measurement, following the same track as **Paper IV**. Since the EIS result is normally interpreted based on a simple planer electrode setup, with the same assumptions as in the GITT method, an updated interpretation when the EIS is used in Li-ion batteries with porous electrode materials would bring a better insight. When it comes to the measurement techniques, an on-board implementation of EIS was demonstrated in **Paper V**. If this method can be implemented continuously throughout the lifetime

of the vehicle, its feasibility for aging diagnostic will be fully verified. In the same way as for the EIS method, the ICI method has the potential to be implemented on-board and included in a normal charging sequence. To sum up, some of the advanced characterization methods, for example EIS and ICI, can be implemented in the on-board diagnostic system to achieve a better understanding of the battery characteristics under real usage conditions.

APPENDIX A

Equipment specification

Table A.1: Specifications of the test equipment used in this work

Test equipment	Specifications
Cell tester	**PEC ACT0550**
	Voltage range 0-5 V
	Voltage control accuracy ± 0.05% FSD
	Voltage measurement accuracy ± 0.005% FSD
	Input impedance 10 MΩ
	Current range 0-50 A with 4 ranges
	Current control accuracy ± 0.03 % FSD
	Maximum sampling frequency 1000 Hz
	On-board input with PT100 temperature sensor
	PEC AIOS
	Type K thermocouples
	Analog voltage input ± 10V 16 bits
	Digital output 10-24 V with maximum 4 A output
Potentiostat	**GAMRY Reference 3000AE**
	Power rang ±32 V/±1.5 A or ±15 V/±3 A

	11 Current ranges (300 pA to 3 A) EIS 1 MHz - 10 μHz Input impedance > 100TΩ || <0.2 pF Sampling frequency up to 1 kHz with modified software **Auxiliary Electrometer** 8 independent channels Voltage input $\pm$5 V Common mode voltage up to $\pm$36 V **Reference 30k Booster** $\pm$30 A EIS up to 300 kHz
DAQ	**Ipetronik M-sens 8 and M-sens 2** Voltage range $\pm$0.1-100 V with 11 ranges 16 bits ADC Sensor excitation 2.5 V to 15 V, max 45 mA Unipolar excitation for M-sens 2, bipolar for M-sens 8 Input impedance 10 MΩ Maximum sampling frequency 2000 Hz CAN interface **Ipetronik M-THERMO 16 and M-THERMO 8** Type K thermocouple Maximum sampling frequency 20 Hz CAN interface **HP/Agilent 34401A** Voltage range 0-1000 V RS232 and GPIB interface
Climate chamber	**Espec LU124** Controlled by PEC server via Ethernet -20 to +85 ^{0}C with $\pm$ 1 ^{0}C fluctuation
Additional heat source	**Omega film flexible heater KHA-508/10** 400 W @ 115 V size 17.7 cm $\times$ 20.3 cm powered with adjustable bench DC power supply
Force sensor	**Load cell TE FC2311-0000-0500-L** 0-500 lbf = 0-2224 newton 5 V power supply 0-100 mV output voltage

Distance sensor	**Laser cell Baumer OM70-L0070.HH0065** 30-70 mm, adjustable window. 1 μm resolution 28 V power supply 0-10 V output voltage Analog and RS485 interface

APPENDIX B

Experimental results

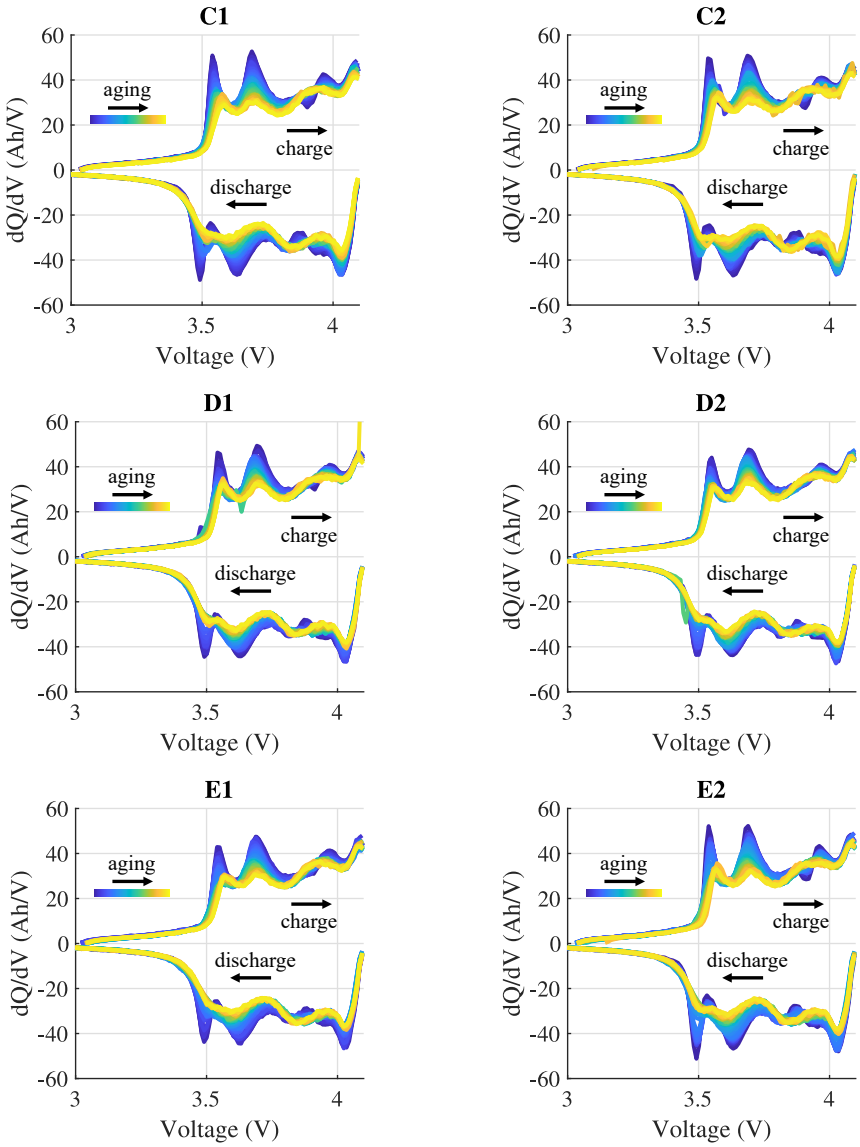

Figure B.1: The incremental capacity analysis (ICA) of Cell C1, C1, D1, D2, E1, and E2.

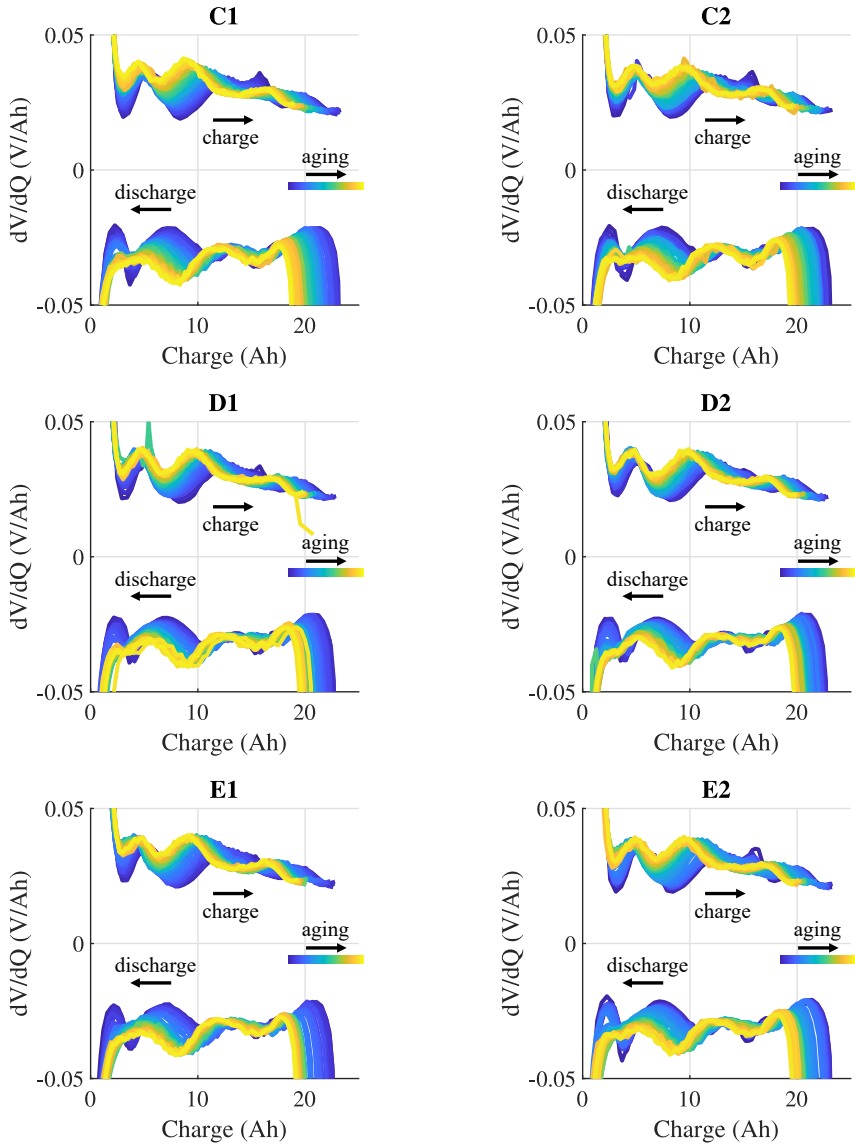

Figure B.2: The differential voltage analysis (DVA) of Cell C1, C1, D1, D2, E1, and E2.

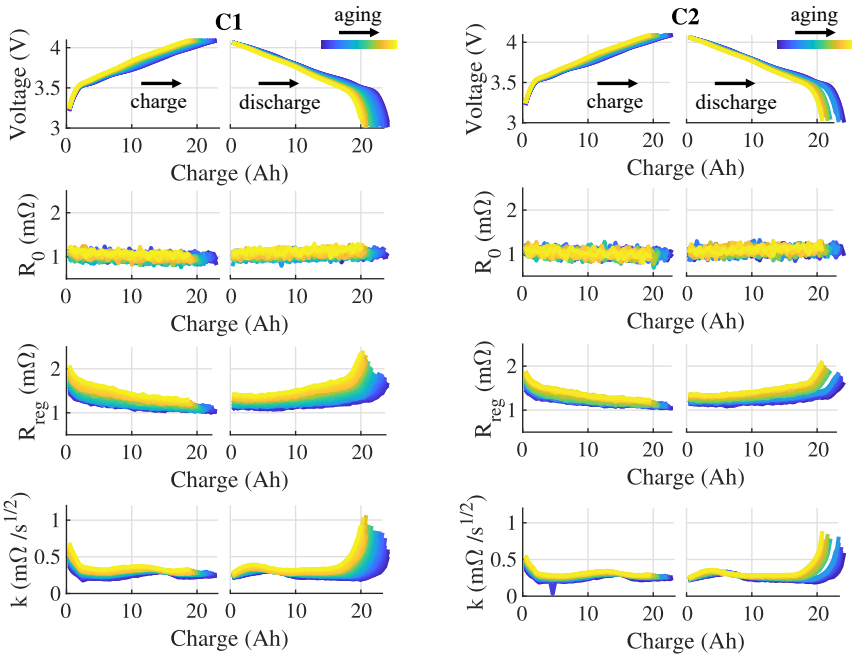

Figure B.3: The ICI regression resistance R_{reg} and diffusive resistance k of Cell C1 and C2.

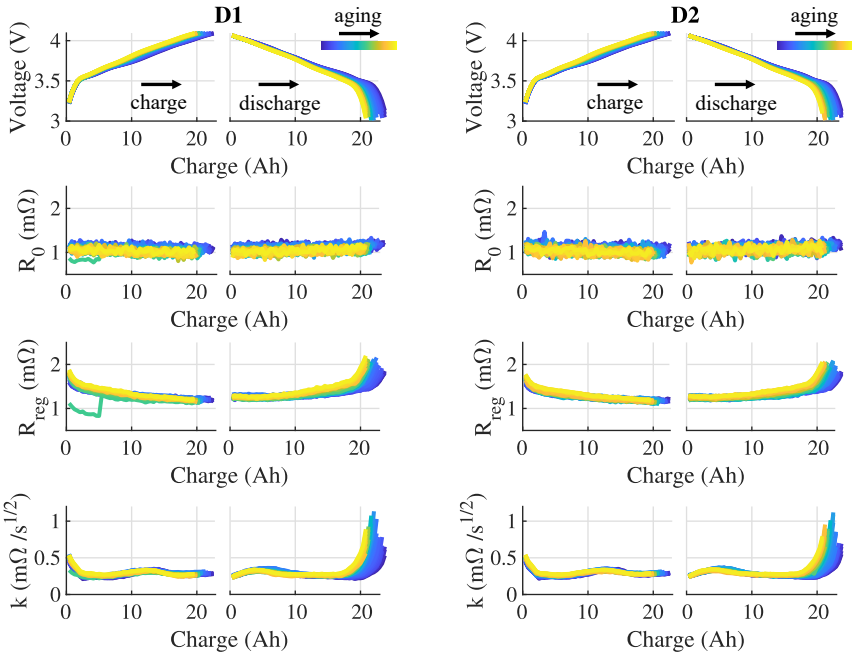

Figure B.4: The ICI regression resistance R_{reg} and diffusive resistance k of Cell D1 and D2.

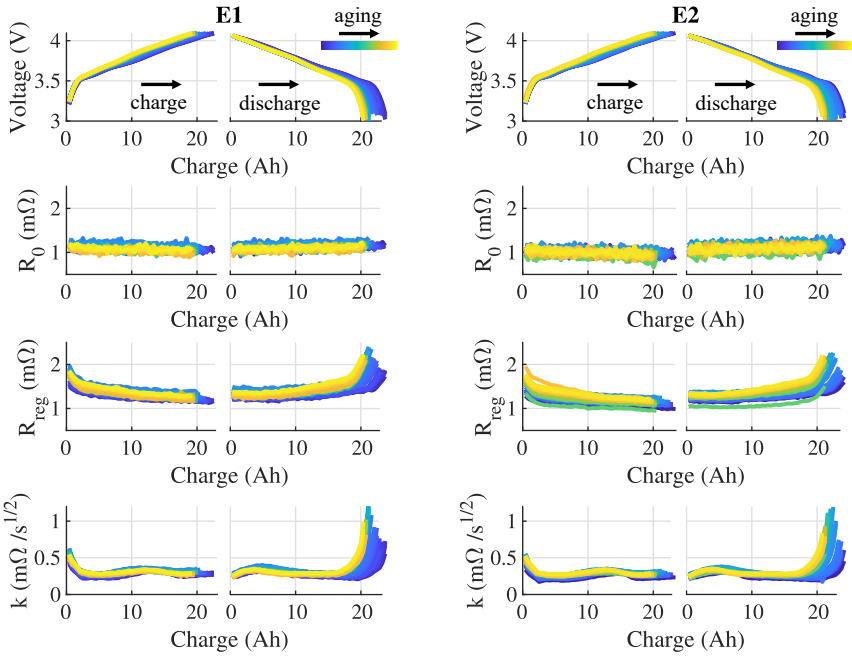

Figure B.5: The ICI regression resistance R_{reg} and diffusive resistance k of Cell E1 and E2.

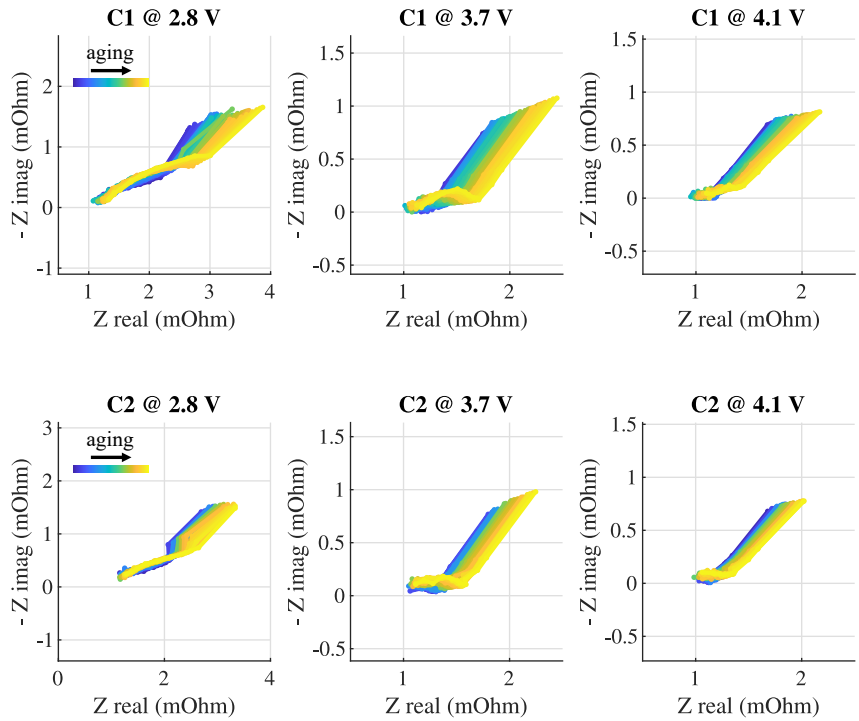

Figure B.6: The EIS measurements of Cell C1 and C2.

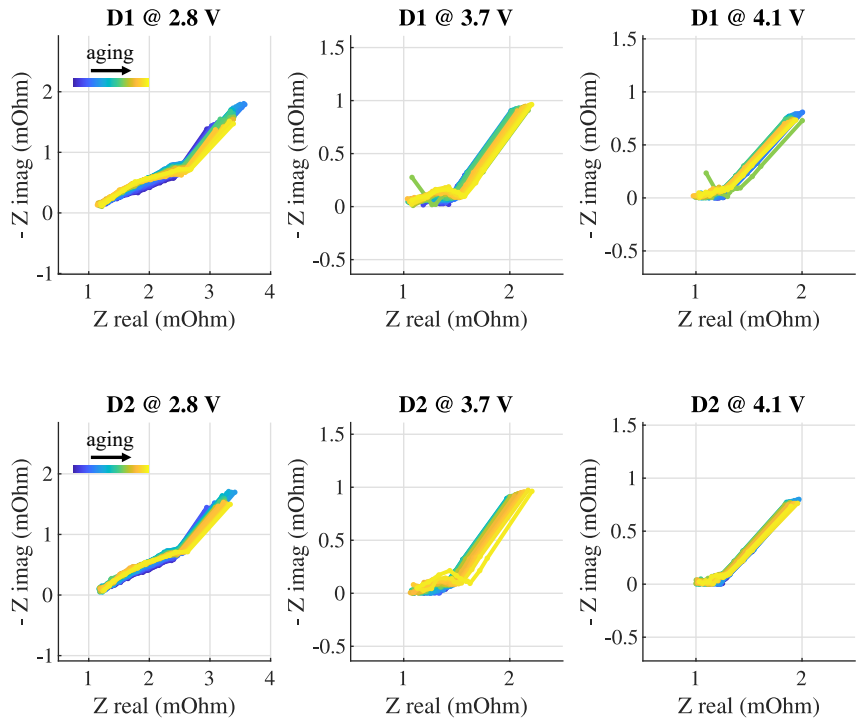

Figure B.7: The EIS measurements of Cell D1 and D2.

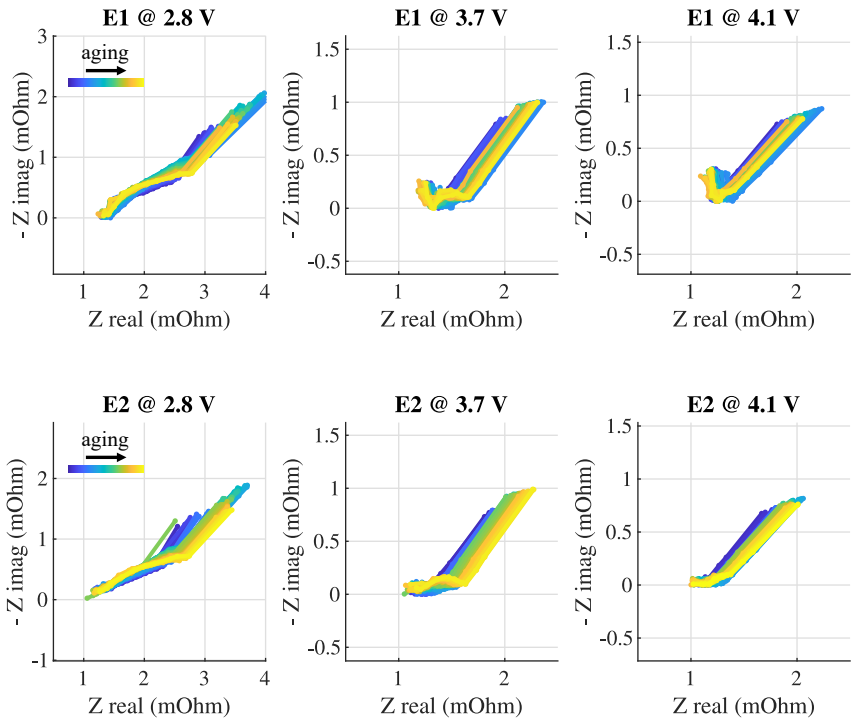

Figure B.8: The EIS measurements of Cell E1 and E2.

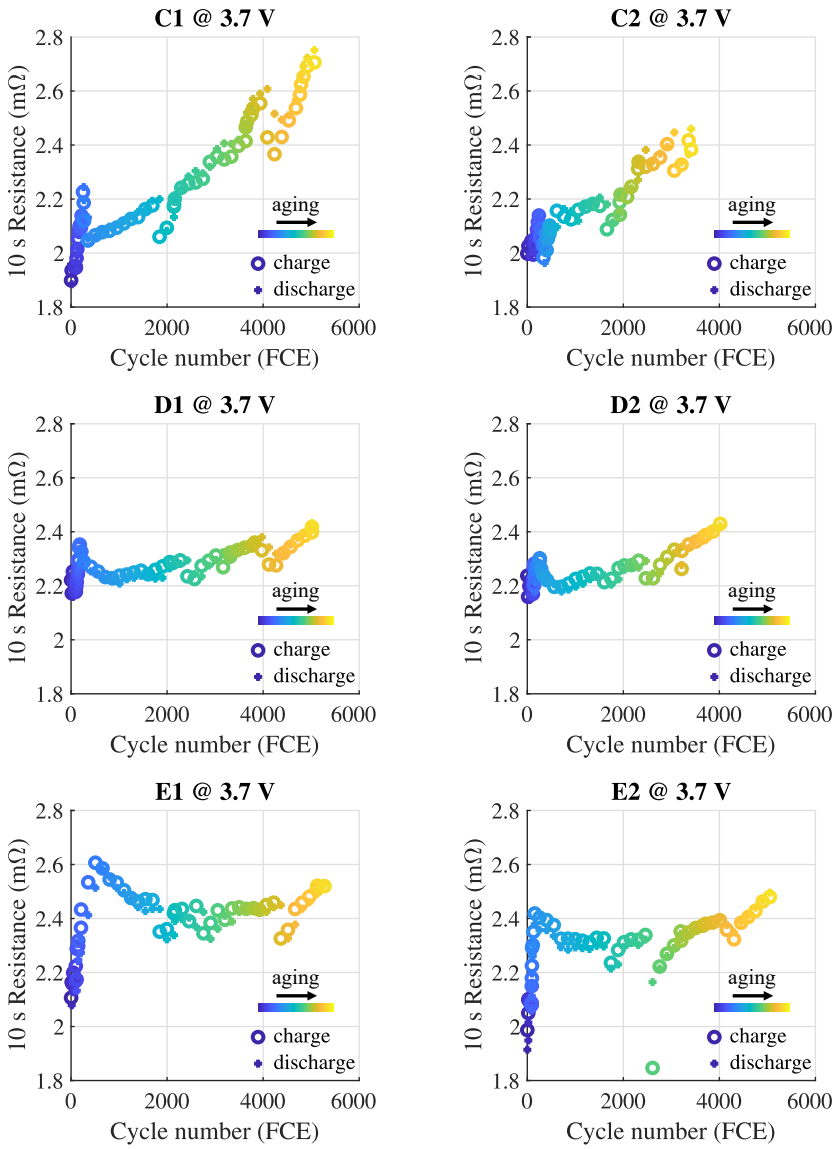

Figure B.9: The 10 second 2C pulse resistance of Cell C1, C1, D1, D2, E1, and E2.

References

[1] M.-T. F. Rodrigues, F. N. Sayed, H. Gullapalli, and P. M. Ajayan, "High-temperature solid electrolyte interphases (SEI) in graphite electrodes," *Journal of Power Sources*, vol. 381, pp. 107–115, 2018.

[2] J. Jaguemont, L. Boulon, P. Venet, Y. Dubé, and A. Sari, "Lithium-ion battery aging experiments at subzero temperatures and model development for capacity fade estimation," *IEEE Transactions on Vehicular Technology*, vol. 65, no. 6, pp. 4328–4343, 2015.

[3] F. Leng, C. M. Tan, and M. Pecht, "Effect of temperature on the aging rate of Li ion battery operating above room temperature," *Scientific reports*, vol. 5, no. 1, pp. 1–12, 2015.

[4] E. Wikner, *Lithium ion battery aging: battery lifetime testing and physics-based modeling for electric vehicle applications*. Chalmers Tekniska Hogskola (Sweden), 2017.

[5] T. Waldmann, M. Wilka, M. Kasper, M. Fleischhammer, and M. Wohlfahrt-Mehrens, "Temperature dependent ageing mechanisms in lithium-ion batteries–a post-mortem study," *Journal of Power Sources*, vol. 262, pp. 129–135, 2014.

[6] V. Smet, F. Forest, J.-J. Huselstein, *et al.*, "Ageing and failure modes of igbt modules in high-temperature power cycling," *IEEE transactions on industrial electronics*, vol. 58, no. 10, pp. 4931–4941, 2011.

[7] E. Ugur, F. Yang, S. Pu, S. Zhao, and B. Akin, "Degradation assessment and precursor identification for SiC mosfets under high temp cycling," *IEEE Transactions on Industry Applications*, vol. 55, no. 3, pp. 2858–2867, 2019.

[8] A. Griffo, I. Tsyokhla, and J. Wang, "Lifetime of machines undergoing thermal cycling stress," in *2019 IEEE Energy Conversion Congress and Exposition (ECCE)*, IEEE, 2019, pp. 3831–3836.

[9] N. Wassiliadis, J. Schneider, A. Frank, *et al.*, "Review of fast charging strategies for lithium-ion battery systems and their applicability for battery electric vehicles," *Journal of Energy Storage*, vol. 44, p. 103 306, 2021.

[10] X.-G. Yang, T. Liu, Y. Gao, *et al.*, "Asymmetric temperature modulation for extreme fast charging of lithium-ion batteries," *Joule*, vol. 3, no. 12, pp. 3002–3019, 2019.

[11] M. Doyle, T. F. Fuller, and J. Newman, "Modeling of galvanostatic charge and discharge of the lithium/polymer/insertion cell," *Journal of the Electrochemical society*, vol. 140, no. 6, p. 1526, 1993.

[12] J. Vetter, P. Novák, M. R. Wagner, *et al.*, "Ageing mechanisms in lithium-ion batteries," *Journal of power sources*, vol. 147, no. 1-2, pp. 269–281, 2005.

[13] X. Han, M. Ouyang, L. Lu, J. Li, Y. Zheng, and Z. Li, "A comparative study of commercial lithium ion battery cycle life in electrical vehicle: Aging mechanism identification," *Journal of Power Sources*, vol. 251, pp. 38–54, 2014.

[14] M. B. Pinson and M. Z. Bazant, "Theory of SEI formation in rechargeable batteries: Capacity fade, accelerated aging and lifetime prediction," *Journal of the Electrochemical Society*, vol. 160, no. 2, A243, 2012.

[15] A. Andersson, D. Abraham, R. Haasch, S. MacLaren, J. Liu, and K. Amine, "Surface characterization of electrodes from high power lithium-ion batteries," *Journal of The Electrochemical Society*, vol. 149, no. 10, A1358, 2002.

[16] P. Keil, S. F. Schuster, J. Wilhelm, *et al.*, "Calendar aging of lithium-ion batteries," *Journal of The Electrochemical Society*, vol. 163, no. 9, A1872, 2016.

[17] Y. Qi, Q. Xu, and A. Van der Ven, "Chemically induced crack instability when electrodes fracture," *Journal of the Electrochemical Society*, vol. 159, no. 11, A1838, 2012.

[18] Z. Geng, T. Thiringer, Y. Olofsson, J. Groot, and M. West, "On-board impedance diagnostics method of Li-ion traction batteries using pseudo-random binary sequences," in *2018 20th European Conference on Power Electronics and Applications (EPE'18 ECCE Europe)*, IEEE, 2018, P–1.

[19] Y.-C. Chien, H. Liu, A. S. Menon, W. R. Brant, D. Brandell, and M. J. Lacey, "A fast alternative to the galvanostatic intermittent titration technique," 2021.

[20] M. J. Lacey, "Influence of the electrolyte on the internal resistance of lithium- sulfur batteries studied with an intermittent current interruption method," *ChemElectroChem*, vol. 4, no. 8, pp. 1997–2004, 2017.

[21] Y. Reynier, R. Yazami, and B. Fultz, "The entropy and enthalpy of lithium intercalation into graphite," *Journal of Power Sources*, vol. 119, pp. 850–855, 2003.

[22] Y. Wu and A. Jossen, "Entropy-induced temperature variation as a new indicator for state of health estimation of lithium-ion cells," *Electrochimica Acta*, vol. 276, pp. 370–376, 2018.

[23] A. Swiderska-Mocek, E. Rudnicka, and A. Lewandowski, "Temperature coefficients of Li-ion battery single electrode potentials and related entropy changes–revisited," *Physical Chemistry Chemical Physics*, vol. 21, no. 4, pp. 2115–2120, 2019.

[24] H. Wang, S. C. Kim, T. Rojas, *et al.*, "Correlating Li-ion solvation structures and electrode potential temperature coefficients," *Journal of the American Chemical Society*, vol. 143, no. 5, pp. 2264–2271, 2021.

[25] Y.-T. Cheng and M. W. Verbrugge, "Diffusion-induced stress, interfacial charge transfer, and criteria for avoiding crack initiation of electrode particles," *Journal of the Electrochemical Society*, vol. 157, no. 4, A508, 2010.

[26] P. Pietsch, D. Westhoff, J. Feinauer, *et al.*, "Quantifying microstructural dynamics and electrochemical activity of graphite and silicon-graphite lithium ion battery anodes," *Nature communications*, vol. 7, no. 1, pp. 1–11, 2016.

[27] C. Birkenmaier, B. Bitzer, M. Harzheim, A. Hintennach, and T. Schleid, "Lithium plating on graphite negative electrodes: Innovative qualitative and quantitative investigation methods," *Journal of The Electrochemical Society*, vol. 162, no. 14, A2646, 2015.

[28] J. Groot, "Snabbladdning av stora energi-optimerade lithiumjonceller för elektriska drivlinor," Tech. Rep., 2018, pp. 2015–002 159.

[29] B. Epding, B. Rumberg, H. Jahnke, I. Stradtmann, and A. Kwade, "Investigation of significant capacity recovery effects due to long rest periods during high current cyclic aging tests in automotive lithium ion cells and their influence on lifetime," *Journal of Energy Storage*, vol. 22, pp. 249–256, 2019.

[30] J. Wilhelm, S. Seidlmayer, P. Keil, *et al.*, "Cycling capacity recovery effect: A coulombic efficiency and post-mortem study," *Journal of Power Sources*, vol. 365, pp. 327–338, 2017.

[31] J. Groot, M. Swierczynski, A. I. Stan, and S. K. Kær, "On the complex ageing characteristics of high-power LiFePO4/graphite battery cells cycled with high charge and discharge currents," *Journal of Power Sources*, vol. 286, pp. 475–487, 2015.

[32] J. Groot, *State-of-health estimation of Li-ion batteries: Cycle life test methods*. Chalmers Tekniska Hogskola (Sweden), 2012.